Gravity Wave Observations by the Mars Science Laboratory REMS Pressure Sensor and Comparison with Mesoscale Atmospheric Modeling with MarsWRF

Scott D. Guzewich[1], Manuel de la Torre Juárez[2], Claire E. Newman[3], Emily Mason[4,1,9], Michael D. Smith[1], Nina Miller[5], Alain S.J. Khayat[6,1,9], Henrik Kahanpää[7], Daniel Viúdez-Moreiras[8], Mark I. Richardson[3]

[1]NASA Goddard Space Flight Center, Greenbelt, MD, USA 20771
[2]Jet Propulsion Laboratory/California Institute of Technology, Pasadena, CA, USA, 91109
[3]Aeolis Research, Chandler, AZ, USA, 85224
[4]University of Maryland Baltimore County, Baltimore, MD, USA 21250
[5]University of Nevada Reno, Reno, NV, USA 89557
[6]University of Maryland College Park, College Park, MD, USA, 20742
[7]Aalto University School of Electrical Engineering, Espoo, Finland
[8]Centro de Astrobiología (INTA-CSIC), Torrejón de Ardoz, Spain
[9]Center for Research and Exploration in Space Science and Technology, NASA/GSFC, Greenbelt, MD, USA 20771

ABSTRACT

Surface pressure measurements on Mars have revealed a wide variety of atmospheric phenomena. The Mars Science Laboratory Rover Environmental Monitoring Station pressure sensor dataset is now the longest duration record of surface pressure on Mars. We use the first 2580 martian sols, nearly 4 Mars years, of measurements to identify atmospheric pressure waves with periods of tens of minutes to hours using wavelet analysis on residual pressure after the tidal harmonics are removed. We find these waves have a clear diurnal cycle with strongest activity in the early morning and late evening and a seasonal cycle with the strongest waves in the second half of the martian year (L_s = 180-360°). The strongest such waves of the entire mission occurred during the Mars Year 34 global dust storm. Comparable atmospheric waves are identified using atmospheric modeling with the MarsWRF general circulation model in a "nested" high spatial resolution mode. With the support of the modeling, we find these waves best fit the expected properties of inertia-gravity waves with horizontal wavelengths of O(100s) of km.

PLAIN LANGUAGE SUMMARY

Measuring air pressure from the surface of Mars has revealed a wide variety of atmospheric phenomena. The Curiosity rover's record or surface air pressure is now the longest yet made on Mars. We use the first ~8 years of Curiosity's pressure observations to look for atmospheric waves with periods of tens of minutes to hours. We find these waves have a clear pattern in their daily behavior with the strongest activity in the early morning and late evening and a seasonal cycle with the strongest waves in the second half of the martian year (Northern hemisphere fall and winter). The strongest such waves occurred in 2018 during a global dust storm. We find comparable waves in atmospheric modeling. With the support of modeling, we find these waves best fit the expected properties of buoyancy waves forced by airflow over topography with horizontal wavelengths of 100-1000 km.

1. INTRODUCTION

Long duration monitoring of atmospheric pressure on Mars has allowed a cornucopia of phenomena to be identified and studied. The Viking lander pressure records serve as the foundation for understanding how CO_2 cycles into and out of the seasonal polar ice caps and how martian dust storms drive variations in atmospheric tides (Martínez et al., 2017; Rafkin et al., 2017; Zurek and Leovy, 1981; Hourdin et al., 1993; Wilson and Hamilton, 1996). Additionally, their location in the northern hemisphere lowlands exposed the Viking Landers to seasonal baroclinic [Barnes, 1980; Tilman, 1988; Collins et al., 1996] and barotropic traveling waves, analogous to terrestrial weather fronts and low pressure storm systems (e.g., Wilson et al., 2002).

The Mars Science Laboratory (MSL) Rover Environmental Monitoring Station (REMS) pressure sensor has now measured the longest record of atmospheric pressure on Mars,

complementing the Viking record due to its near-equatorial southern hemisphere location. The REMS pressure sensor has detected the seasonal CO_2 cycle and the familiar atmospheric tides [Haberle et al., 2014; Guzewich et al., 2016]. Its finer resolution compared to the pressure sensors carried by the Viking landers has even permitted the detection of distant baroclinic traveling waves, which originate at high latitudes and have very low amplitudes by the time they reach MSL's location [Haberle et al., 2018]. The 1 Hz measurement rate has also allowed the detection of much more transient phenomena, such as pressure dips associated with passing convective vortices [e.g., Steakley and Murphy, 2016; Kahanpää et al., 2016; Ordonez-Exteberria et al. 2018; Ordonez-Exteberria et al. 2020; Newman et al. 2019; Kahanpää and Viúdez-Moreiras, 2020], which if sufficiently dusty may be visualized as 'dust devils.' MSL's location within Gale Crater has also shown how the topography forces atmospheric flows that maintain hydrostatic balance [Richardson and Newman, 2018], the planetary boundary layer [Tyler and Barnes, 2015], and wavelike perturbations with periods of tens of seconds to minutes likely driven by topographic wind flows and/or gravity waves forced by the topography of Gale Crater [Harri et al., 2014; Haberle et al., 2014; Ullán et al., 2017]. More recently, the InSight lander, with a sensitive pressure sensor that obtains measurements at much higher rate (up to 20 Hz), has detected undular bores, infrasound, and gravity waves with periods of minutes [Banfield and Spiga et al., 2020].

This work is motivated, in part, by two factors. First, we aim to search for atmospheric behavior with periods of tens of minutes to hours. This is a region of the time domain that is previously not well-studied on Mars from surface meteorological stations. Second, the visual observation of gravity wave-like behavior in water ice clouds seen above Gale Crater by Kloos et al. [2018]. These cloud patterns are consistent with temperature moving alternately above and

35 below the water ice condensation temperature due to gravity waves, and we seek to determine
36 whether such temperature or pressure variability is measured on the surface by REMS.
37 Based on modeling and theory of both Earth and Mars, we suggest that atmospheric
38 waves with periods of tens of minutes to hours (and with frequencies greater than the inertial
39 frequency) should primarily be inertia-gravity waves. Inertia-gravity waves have sufficient
40 horizontal wavelengths to be impacted by the rotation of the planet through the Coriolis effect
41 and have buoyancy act as the restoring force to a vertical displacement. Of course, at the near-
42 equatorial location of Gale Crater, the Coriolis forcing is minimal. They can be caused by a
43 variety of mechanisms under statically stable conditions including flow over topography,
44 atmospheric convection, and wind shear near atmospheric jets and fronts (e.g., Plougonven and
45 Zhang, 2014). Given their long horizontal wavelengths, their sources could be far from Gale
46 Crater. On Earth, gravity waves have been detected by surface pressure sensors, from a variety
47 of forcing mechanisms (e.g., Marlton et al., 2015), while on Mars they may have been detected
48 in surface pressure readings from orbiting spacecraft [Spiga et al., 2007], entry, descent, and
49 landing profiles of temperature [Magalhães et al., 1999], and airglow imagery [Altieri et al.,
50 2012] (among other methods). Furthermore, as already mentioned, perturbations possibly caused
51 by gravity waves have been detected in the surface pressure records of MSL and InSight, albeit
52 with shorter time scales than studied in this work [Harri et al., 2014; Haberle et al., 2014; Ullán
53 et al., 2017; Banfield and Spiga et al., 2020]. More commonly for Earth and Mars, gravity waves
54 are detected in limb-viewing geometries as perturbations to the vertical temperature structure [de
55 la Torre and Alexander, 1995, 2005; Creasey et al., 2006; Heavens et al., 2020]. As they
56 propagate horizontally and vertically, they alter the thermal structure of the atmosphere (e.g.,
57 Creasey et al., 2006; Kuroda et al., 2015; Gilli et al., 2019) and breaking waves deposit

momentum into the circulation, slowing or speeding winds (e.g., Gossard and Munk, 1954; Bretherton, 1966 and references therein).

In this work, our analysis predominantly focusesd on atmospheric pressure and temperature. Section 2 describes the REMS observations in addition to general circulation modeling using the MarsWRF atmospheric model that was performed to complement our data analysis. Section 3 presents detections of inertia-gravity waves with periods of tens of minutes to hours in REMS pressure observations and non-detections in concurrent temperature observations, Section 4 provides some contextual discussion and concludes.

2. METHODOLOGY

2.1. REMS Observations

In this work we have used REMS pressure and temperature observations from the first 2580 sols (martian solar days), nearly 4 Mars years, of the MSL mission. Wind measurements would be ideal for wave detections, but the REMS wind sensors failed near mission Sol 1500 and were only able to detect winds coming from the rover's pointing direction prior to that [Viúdez-Moreiras et al., 2019]. Gómez-Elvira et al. (2012) and Harri et al. (2014) provide overviews of the REMS instrument and its performance. REMS takes observations at a frequency of 1 Hz during the first 5 minutes of every Local Mean Solar Time (LMST) hour, as well as during up to eight hours of "extended block" observations per sol. This cadence was created to manage the instrument's power and data budgets, while providing maximum diurnal coverage. These extended blocks consist of (i) 1-hour observations every 6 hours, shifting an hour earlier each sol, hence covering a full diurnal cycle every 6 sols, and (ii) 3-hour observations that cover the same 3 hours for 3 sols before shifting 3 hours earlier, hence cover a full diurnal cycle in 3-hour blocks every 24 sols. The hour surrounding local solar noon is also

observed on nearly every sol, due to the expected peak of UV radiation and coinciding with the maximum convective vortex activity at that time-of-day (e.g., Miller et al., 2018; Newman et al., 2019). Newman et al. (2017) and Guzewich et al. (2019) show examples of the REMS observation cadence. We convert all observations to local true solar time (LTST) for analysis.

Harri et al. (2014) provides a thorough overview of the accuracy and precision of the REMS pressure measurements. In isolation, the resolution of the pressure sensors is ~0.2 Pa, limited by the noise level. Larger uncertainties associated with the sensor warmup period (1 s), response time (1 s), shadowing by the rover's remote sensing mast (max. 1 Pa drop), and repeatability variation (induced by hysteresis with respect to the sensor's temperature, varying on the timescale of a sol; < 1.5 Pa) are also detailed by Harri et al. (2014). We focus on searching for waves with periods of tens of minutes to hours and therefore combine individual REMS measurements into 30-second averages for our analysis. This strongly mitigates the instrumental effects of noise, response time, sensor warmup, and the "shadow effect". In nominal measurements, the REMS pressure instrument outputs readings of two Vaisala Barocap® sensor heads with different temperature hysteresis (Harri et al., 2014). We have repeated some of our analysis using data from each of these two Barocap® sensor heads independently and found no indications of the repeatability variation influencing our results. Lastly, we have removed time periods (~every 100 sols) when pressure sensor self-checks have been performed and data are not fully comparable (Harri et al., 2014). In total, we assume we are able to resolve atmospheric waves with amplitudes of 0.2 Pa.

The Curiosity rover has traversed over 20 km of horizontal distance and several hundred meters of vertical elevation during its roughly 9 Earth year/4.5 Mars year surface mission to date. We do not normalize the pressure to a single altitude as it is plausible that wave behavior could

105 change based on elevation or horizontal position and because elevation changes are negligible
106 within a single sol (during which we remove the pressure harmonics, see below) or even within
107 the 10-sol periods we typically analyze (see below). Our 1-10 sol analysis periods also remove
108 the signature of the martian seasonal pressure cycle, driven by the condensation / sublimation of
109 CO_2 onto / off the polar ice caps in autumn and winter / spring and summer (see figure 1 by
110 Haberle et al., 2018).

111 After combining REMS measurements into 30-second averages, our analysis proceeds by
112 fitting and then subtracting a low-order harmonic to a single sol's pressure or temperature data.
113 We select here eight harmonics for the fit, which effectively removes the low-order frequencies
114 (Figure 1) produced by the atmospheric tides (e.g., Haberle et al., 2014; Guzewich et al., 2016)
115 and the effect of the hydrostatic adjustment flows (Richardson and Newman, 2018). These
116 mechanisms are responsible for the vast majority of the daily surface pressure variability on
117 Mars, particularly at equatorial locations like Gale Crater.

118 Figure 1 shows an example of the harmonic fitting procedure. We assume the
119 atmospheric tides and other mechanisms affecting the pressure variability along the sol such as
120 the effect of the hydrostatic adjustment flows are harmonics of the solar day as in Equation 1:

121 $$p(t) = p_o + \Sigma_{k=1}^{n} A_k cos(2\pi kt) + B_k sin(2\pi kt) \quad (1)$$

122 where $p(t)$ is pressure as a function of time, p_o is the mean pressure, k is the numbered
123 harmonic, n is the total number of harmonics considered in the fit (n=8 for this study), and t is
124 time. The amplitudes of the harmonics, A_k and B_k, are found through singular value
125 decomposition of the matrix filled with the trigonometric functions.

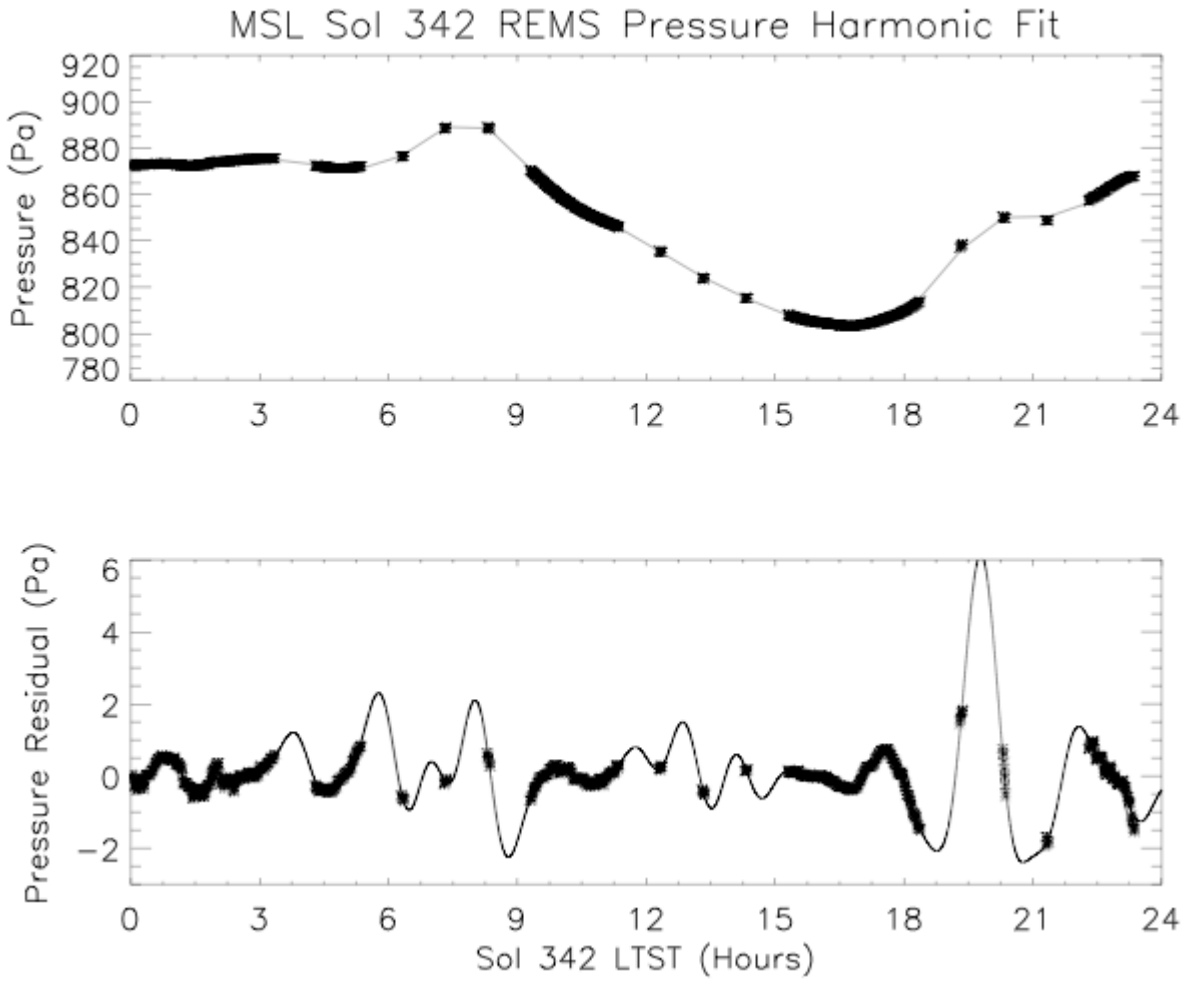

Figure 1. (Top) REMS pressure observations for MSL Sol 342 (asterisks) and low-order harmonic fit (n=8) to it (line). (Bottom) REMS pressure residual (asterisks) and a 24th order harmonic fit to it (line).

In Figure 1, the cadence of REMS hourly or multi-hourly extended blocks and 5-minute background observations can be clearly seen. Removing the harmonic fit leaves a residual pressure variation that is shown in the bottom plot of Figure 1. At this stage, multiple analysis methods are available to examine the wave behavior present. The lower panel of Figure 1 and Figure 2 use a 24^{th} order harmonic fit to the pressure residual to demonstrate wave-like behavior in the pressure residual, but that is not used elsewhere in this work.

All analysis methods shown below indicate that there are frequent waves with periods of ~1-3 hours and amplitudes of O(1-10 Pa) present in Gale Crater that are detectable by REMS. However, we must note that two factors may bias this analysis, regardless of the method we choose.

First, our chosen harmonic fit (specifically the number of harmonics) to remove the pressure tides selects, to some degree, which wave periods remain in the residual pressure after removing the harmonic fit. Our choice of 8 harmonics effectively removes most waves with periods longer than 3 hours and hence we make the implicit choice that non-tidal waves of interest to this analysis will have periods shorter than 3 hours. Note that we do not completely eliminate the ability to detect waves with periods longer than 3 hours (as seen in Section 3.2), but the wave power or amplitude of these waves as depicted is likely weaker (perhaps much weaker) than in reality. Based on our previous analysis of tides in REMS pressure data (e.g., Guzewich et al., 2016), we know that tides up to p_6 (the 6-per-sol tide with a period of 4 hours) are clearly present with amplitude of about 3 Pa that varies with season and atmospheric dust loading and thus 6 harmonics is the bare minimum to effectively remove them. Choosing more harmonics (n=10 or n=12) fits the daily REMS pressure to such a degree that the remaining residual is dominated by variations more likely driven by turbulent boundary layer processes (e.g., convection) that are the subject of future work.

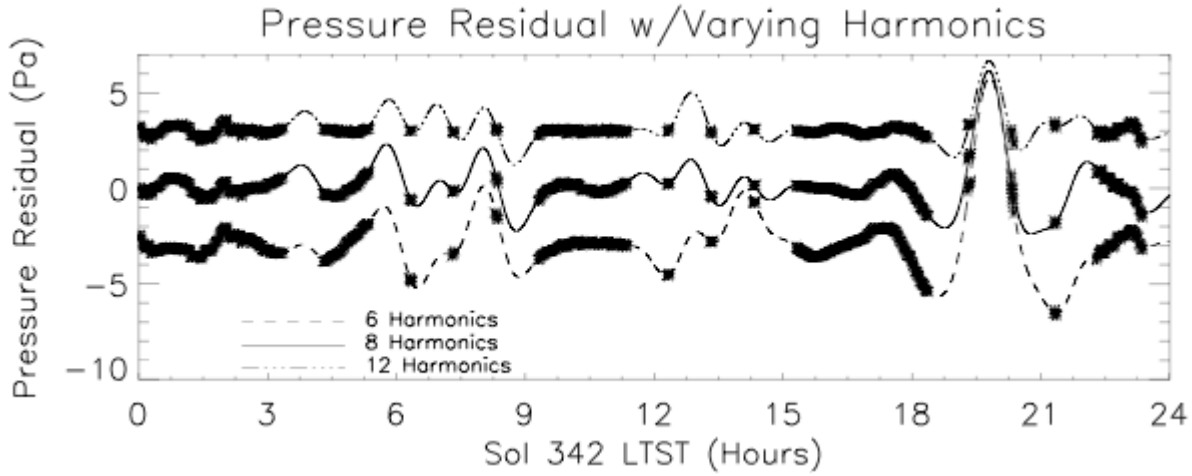

Figure 2: REMS pressure residuals (asterisks) and 24th order harmonic fits to them (lines). The residual after using n=6 in the harmonics fit is offset by -3 Pa and shown with the dashed line, the residual after fitting n=8 is shown by the solid line, and the residual after fitting n=12 is offset by 3 Pa and shown by the dashed-3 dotted line.

In Figure 2, we demonstrate how the pressure residual is modified by the choice of a n=6, 8, or 12 harmonics fit to the Sol 342 REMS pressure observations. The residual with n=6 and n=8 is generally similar, with some increased amplitude in longer-period waves in the former. However, the residual after fitting n=12 is very flat with little variation and the 24th order harmonic fit to the residual is overfit.

Second, the REMS observation cadence likely biases these results to some degree. REMS extended blocks are typically 1-3 hours in duration, with rare extended blocks of 4 or 5 hours duration. Both the harmonic analysis and the wavelet analysis have sensitivity to waves of longer periods, but may be inherently less sensitive to wave periods longer than the typical REMS extended block due to the nature of the observation cadence. We have conducted tests of our wavelet analysis (see below for a further discussion of wavelet analysis) with idealized combinations of wave amplitudes and periods observed at REMS-like cadences and found that the wavelet analysis is still able to correctly identify the wave periods, even if they are longer than typical REMS extended blocks (e.g., 6 hour wave periods) (Figure 3). In the idealized case

175 in Figure 3 (top panel), we created a residual pressure sequence for 10 sols that represents a
176 changing combination of waves with periods of 1, 2, and 6 hours with varying amplitudes. In the
177 bottom panel of Figure 3, we sample that idealized pressure sequence in the same pattern that
178 REMS observed during Sols 2020-2029. It can be seen that some wavelet power "leaks" into
179 adjacent periods and some is aliased into both shorter and longer multiples of a given period.
180 However, the true period is still identifiable in each case. This implies that the predominance of
181 observed wavelet power at periods <3 hours is real and not primarily an artefact of the REMS
182 observation cadence and that we are able to detect wave periods longer than 3 hours.

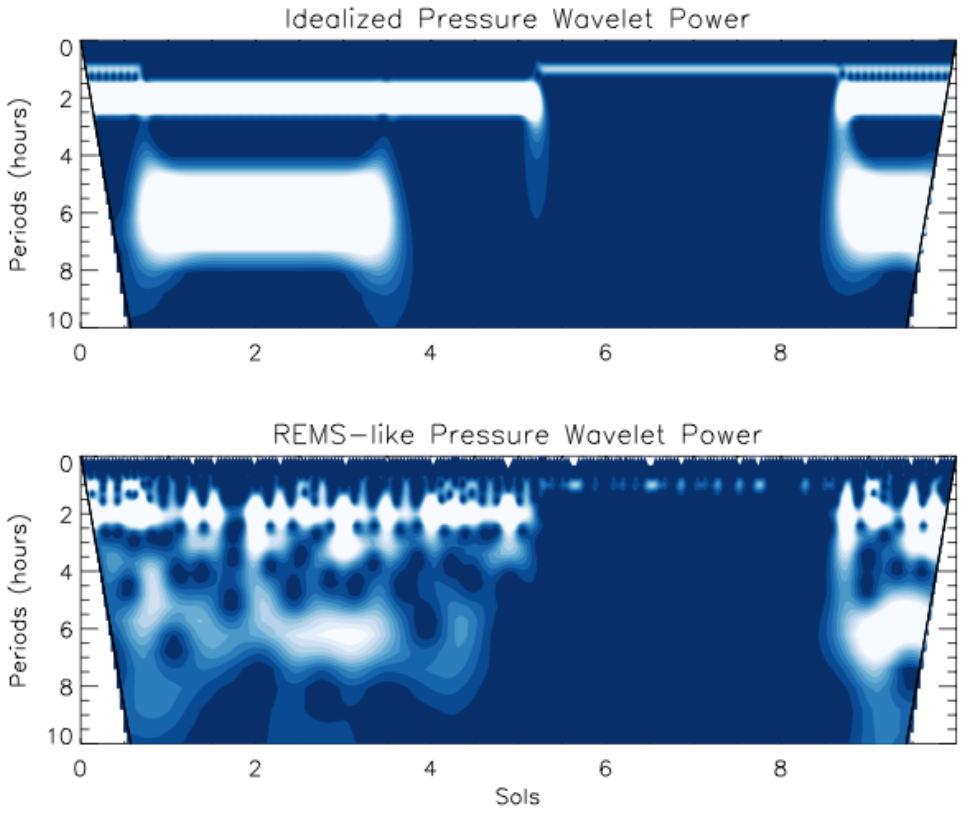

183

184 Figure 3: Wavelet power spectrum for an idealized pressure residual that represents a
185 combination of 1, 2, and 6-hour period waves (top). (Bottom) Wavelet power spectrum for the
186 same idealized pressure residual, but sampled at a cadence following REMS observations during
187 Sols 2020-2029.
188

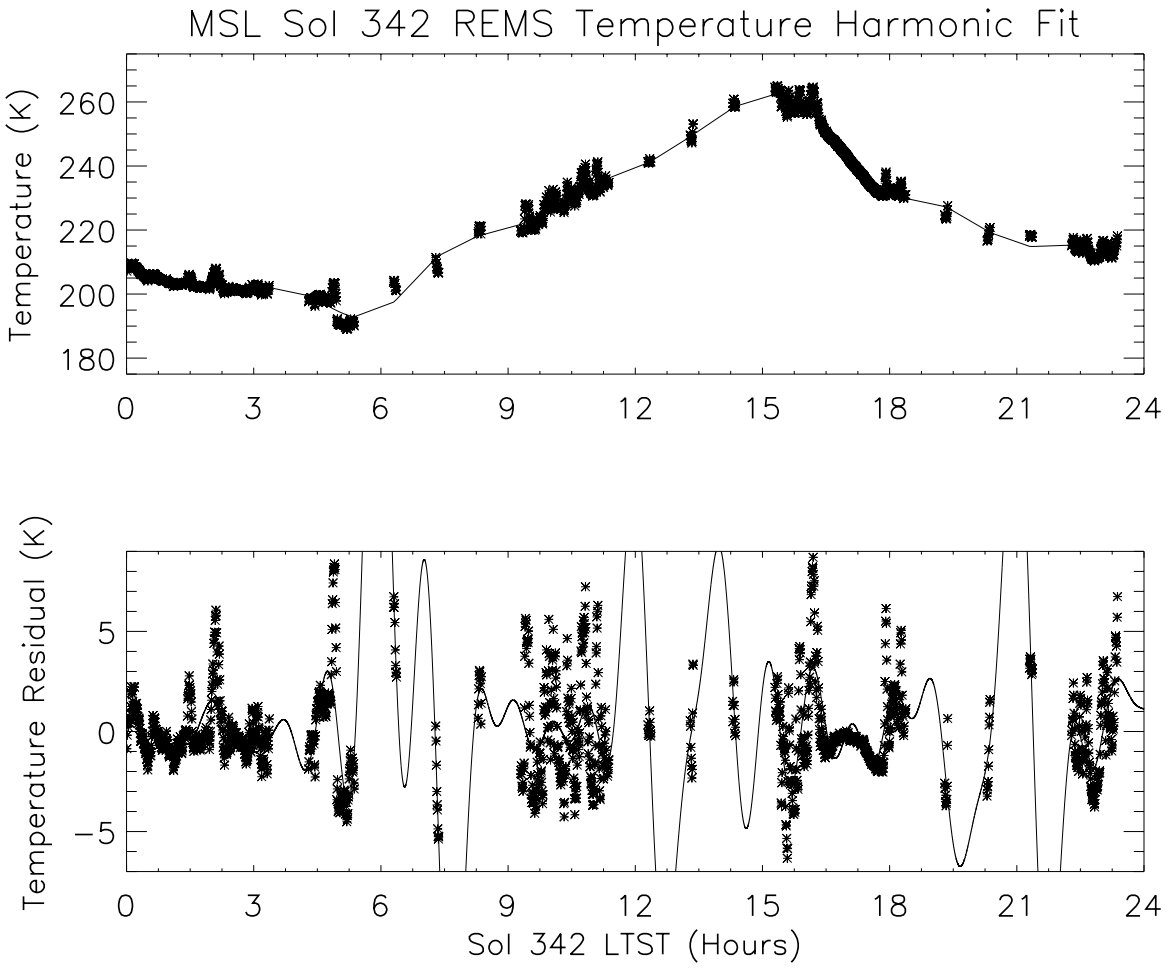

Figure 4. (Top) REMS temperature observations for MSL Sol 342 (asterisks) and 8th order harmonic fit (n=8) to it (line). (Bottom) REMS temperature residual (asterisks) and a 24th order harmonic fit to it (line).

We can conduct the same type of analysis on REMS temperature measurements. Comparing Figures 1 and 4 confirms that the residuals of pressure and temperature behave very differently, due to different physical phenomena driving their variations. Indeed, the 8th-order harmonic fit to temperature generally provides a poorer fit (Figure 4, top panel) than that for pressure (Figure 1, top panel). And while the pressure residual shows clear wavelike behavior and the 24th-order harmonic fit provides a reasonable match to this pressure residual (Figure 1, bottom panel), a 24th-order harmonic fit does not fit the temperature residual well at all. The

temperature variability is much higher frequency/shorter period and higher amplitude (as a fraction of the mean temperature) than that of pressure. These temperature fluctuations are more sensitive to changes in local radiative and topographic forcing mechanisms that drive, largely, turbulence and convective processes superposing them on the underlying large-scale wave forcing (Sutton et al., 1978; Schofield et al., 1997; Smith et al., 2006; Spanovich et al., 2006; Martínez et al., 2009; Mason and Smith, 2021), as is also seen in Figure 5. For this reason, we reserve most additional analysis of these temperature variations to future work, with the exception of Section 3.1 below.

We employ wavelet analysis for the bulk of our analysis of REMS pressure data. Wavelet analysis (Haar, 1910; Calderón, 1960) is a more flexible analysis method, and one that is well-suited to the on-and-off nature of REMS observations. It is particularly advantageous for transitory phenomena and makes no assumption about when a wave begins, ends, or what wave periods are present. Banfield and Spiga et al. (2020) also use wavelet analysis to identify short-period atmospheric waves in InSight pressure observations, although the 20 Hz sampling rate of InSight's pressure sensor opens up an analysis regime that is not available to REMS. We utilize a continuous wavelet transform with an assumed "Morlet" wavelet shape (Torrence and Compo, 1998; wavelet software available at http://paos.colorado.edu/research/wavelets/). We combine REMS observations into ~10-sol groupings of 30-second average values for this analysis, which enables us to detect waves with periods of up to ~48 hours in practice. The "cone of influence" specifies what regions of the period-time phase space are amenable to confident wave detections, and wavelet power outside the cone of influence is ignored. The 30-second periods without REMS observations (i.e., most of each sol, see Figure 1) are assigned pressure perturbations of zero. In essence, a wavelet analysis works by shifting the wavelet shape across the time series of

REMS pressure observations, while adjusting the amplitude and frequency of the wavelet to best fit the observations. The output can be either expressed as amplitude or, more commonly, power (e.g., Banfield and Spiga et al., 2020) as a function of period and time.

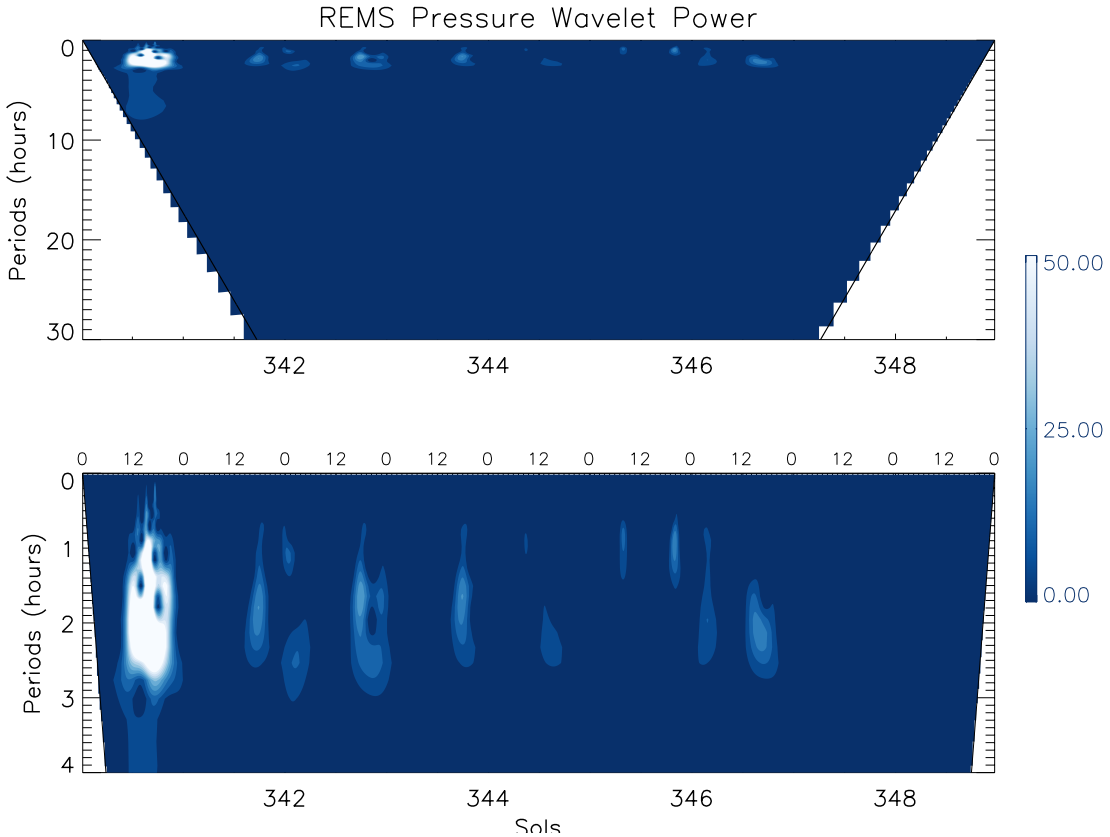

Figure 5. REMS pressure wavelet power (Pa^2) for the Sol 340-349 period. The bottom panel is zoomed in to highlight periods less than 4 hours and local time is labeled on the top abscissa for reference. The cone of influence is represented by the thick black diagonal lines in each panel.

Figure 5 shows an example wavelet power spectrum for the 10-sol period including Sol 342 that has already been showcased in Figures 1 and 4. Nearly all power is contained in wave periods shorter than 3 hours, as expected given our choice of 8 harmonics to fit to the daily pressure curve. A particularly strong wave event, represented by the flame-shaped blob on the left half of the bottom panel of Figure 5, was detected by REMS in the afternoon of Sol 341. Sol

342, which we have already analyzed in Figure 1 using harmonic fitting, shows modest wavelet power in the early morning with periods of ~2.5 hours, no wave activity in the midday, and then a stronger period of wave activity in the late evening with periods of 1.5-2.5 hours. This matches well with what was implied by the harmonic fitting of the pressure residual shown in Figure 1.

2.2. MarsWRF Simulations

We conducted a series of MarsWRF general circulation model (GCM) simulations to compare against and contextualize the REMS observations. MarsWRF has the ability to "nest" higher spatial resolution domains within a lower resolution global domain [Richardson et al., 2007; Newman et al., 2017], enabling the latter to be driven by realistic regional and global scale circulations while also capturing local dynamics, such as mesoscale flows driven by topography. We employ the simulation architecture described by Newman et al. [2017] (vertical grid "B") with a 2° horizontal resolution global domain and a series of nested domains centered over the InSight and MSL landing sites in Elysium Planitia and Gale Crater, respectively. Specifically, we use "Domain 2" and "Domain 3" to provide mesoscale regional information (see Newman et al. [2017] figure 14). For reference, Domain 3 has a spatial resolution of ~13 km at Gale Crater, which allows waves of ~40 km horizontal wavelength to be resolved. We conduct 12 short-duration simulations with the nested domains, starting approximately every 30° of solar longitude and run each simulation for 10 sols. The first sol of each simulation is disregarded for analysis to allow the nest to "spin up". Meteorological variables are output every 10 minutes. For simplicity, we assume a prescribed dust distribution (the "MCD MGS scenario"; Montmessin et al., 2004; Toigo et al., 2012) and no radiatively active water ice clouds.

3. RESULTS

263 3.1. Standard Deviation

264 The most basic analysis step after removal of the low-order harmonic fit (see Section 2.1)
265 to the daily pressure or temperature variation is to take the standard deviation of the difference
266 between the harmonic fit and observed pressure or temperature. This provides an initial first
267 glance at the seasonal and diurnal pressure and temperature variability, but with no information
268 on the cause of the variability or the properties of potential waves.

269

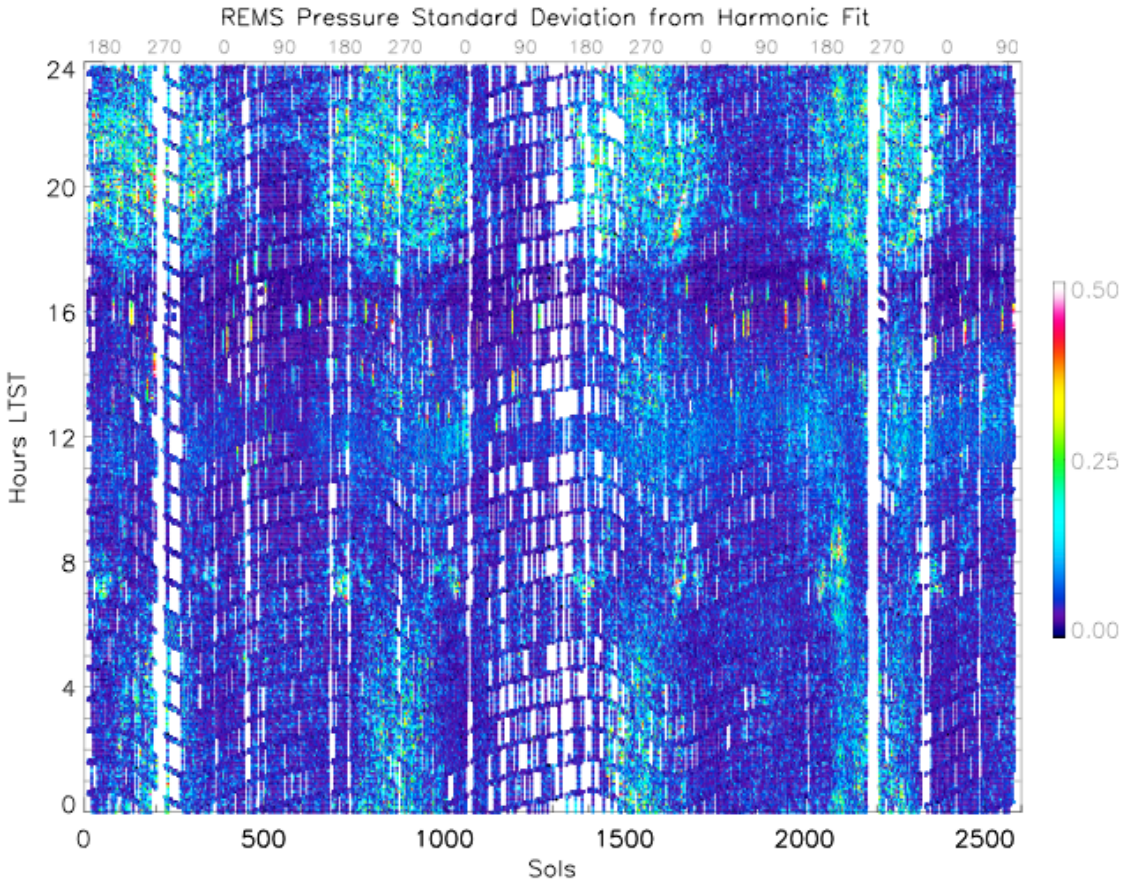

270
271
272 Figure 6. Standard deviation (Pa) of REMS pressure from the daily harmonic fit for the
273 first 2580 sols of the MSL mission. The undulatory sampling in LTST is a consequence of
274 REMS sampling in LMST units and the seasonal change when converting from LMST to LTST.

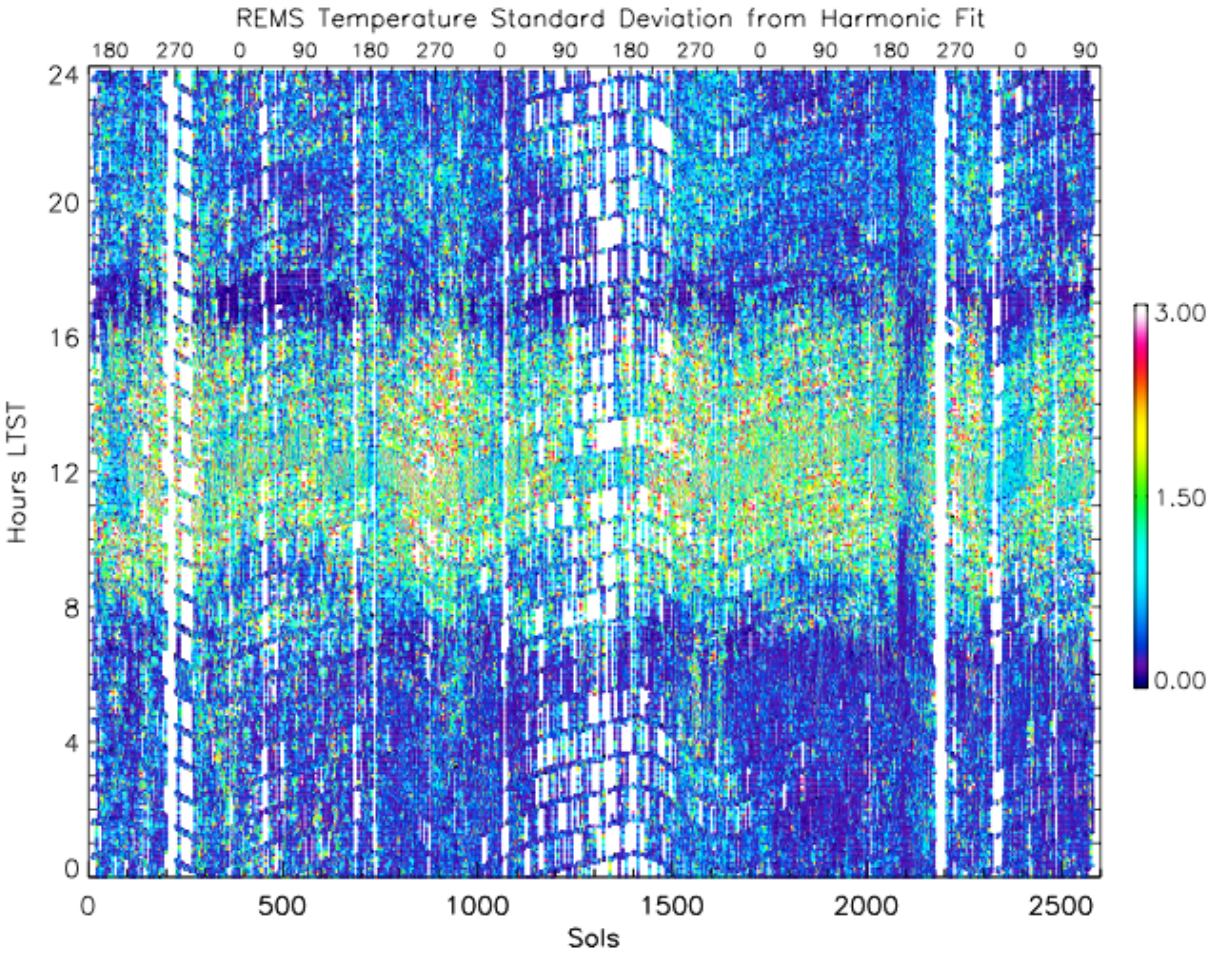

Figure 7. Standard deviation (K) of REMS air temperature from the daily harmonic fit for the first 2580 sols of the MSL mission.

It is immediately apparent by comparing Figures 6 and 7 that the pressure and temperature residuals behave very differently both seasonally and diurnally. The pressure standard deviation (Figure 6) exhibits an annual cycle of increased perturbations (particularly in the late evening, 1700-2400 LTST) beginning at approximately $L_s = 150°$ (the end of southern hemisphere winter, coincidently at the same time of year that Curiosity landed on Mars) and then extending to near or just beyond $L_s = 0°$ (the southern hemisphere autumn equinox). In between those times, pressure deviations from the harmonic fit are minimal. The primary time of day for this pressure activity is in late evening (1700-2400 LTST) and early morning (0000-0500 LTST),

287 rather than during daylight hours. The seasonal cycle of early morning pressure deviations is
288 similar to that in the late evening, but appears to have a somewhat narrow seasonal window with
289 noticeable activity from approximately L_s = 220°-340°. The Mars Year (MY) 34 global dust
290 storm (GDS, MSL Sols 2080-2160, Guzewich et al., 2019; Viúdez-Moreiras et al., 2019) altered
291 this seasonal behavior, particularly for the early morning (0000-0500 LTST) pressure deviations.
292 There is also some weak pressure behavior near solar noon. In all cases, the standard deviations
293 from the pressure harmonic fit are 0.25-0.5 Pa. This is directly comparable to the pressure
294 perturbations shown by Harri et al. [2014], Haberle et al. [2014], and Ullán et al. [2017] believed
295 to be driven by topographic effects including gravity waves. However, as shown below, we
296 isolate pressure behavior with periods that are much longer than identified by those works.
297 As stated above, the temperature behavior is clearly distinct from pressure in most
298 respects. The amplitude of the temperature perturbations is typically 1-3 K. Most temperature
299 deviations occur during daylight hours, centered on or just after solar noon. There is a modest
300 seasonal cycle to the diurnal extent of the daytime temperature perturbations, with the greatest
301 diurnal extent (~0800-1600 LTST) near L_s = 290° each year. As with pressure, there is again
302 some temperature activity in the evening from 1800-2400 LTST that also seems responsive to
303 the dust cycle in a similar way to the coincident pressure cycle, suggesting that both are tied to
304 the same physical process. Morning activity is more modest than that of the evening. Again
305 similarly to pressure, the temperature activity was clearly impacted by the MY34 global dust
306 storm near MSL Sol 2100. The greatly reduced diurnal variability in air and ground temperature
307 during the storm (Guzewich et al., 2019; Viúdez-Moreiras et al., 2019) also appeared to stabilize
308 the perturbations to temperature seen in nearly all other sols of the mission. Throughout the
309 mission, the daytime temperature behavior is consistent with turbulent convection (Miller et al.,

310 2018) and is the expected response to radiative forcing from modeling and known from previous
311 landed missions (Mason and Smith, 2021).

312 Recently, Miller et al. (2018) and Banfield and Spiga et al. (2020) identified a previously
313 unknown atmospheric “quiet” period immediately after sunset and extending for 2-4 hours in
314 pressure and temperature data from both MSL and the InSight lander (also seen in wind
315 measurements by InSight). InSight observations indicate this quiet period has extremely stable
316 pressure observations, with very little variability. This stability is important for InSight’s
317 seismometry mission and this time of day is when most of the Marsquakes observed to-date have
318 been detected (Banfield and Spiga et al., 2020; Clinton et al., 2021). In Figures 6 and 7, we see
319 that such a quiet period is also present within Gale Crater throughout the MSL mission. The
320 quiet period within Gale Crater is most clearly seen in temperature (Figure 7) and immediately
321 follows the turbulent daytime regime with noticeably decreased temperature perturbations. Due
322 to the comparatively weak daytime pressure variability, the quiet regime is less obvious in
323 pressure, but still present.

324

325 3.2. Wavelet Analysis

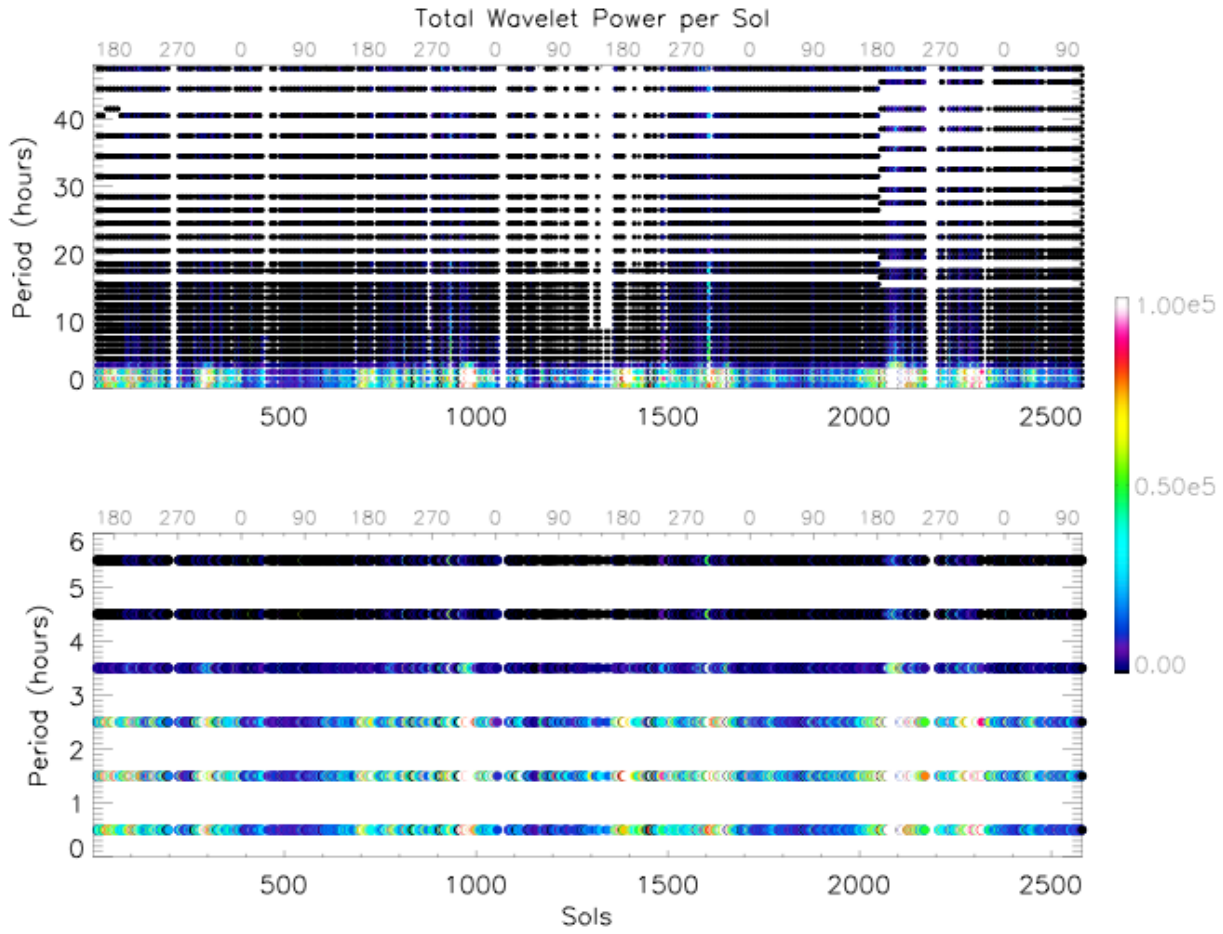

Figure 8. Total wavelet power (Pa^2) per sol for the first 2580 sols of the MSL mission as a function of period (hours). Periods are displayed as centered values in 1-hour intervals (e.g., 0.5 hour period covers periods from 0-1 hour). The bottom plot highlights periods under 6 hours.

The seasonality present in Figure 6 is clear as well in Figure 8. Wavelet power is highest during the dustier seasons (southern spring and summer), with minimal activity during the clearer southern autumn and winter seasons. The seasonality for all wave periods is approximately the same, with some minimal interannual variability present. Interestingly, wavelet power is highest on the edges of the dusty season, with modestly weaker wavelet power at the peak of the dusty season near southern summer solstice. This pattern is analogous to the "solsticial pause" seen in traveling wave behavior (Wilson et al., 2002; Lewis et al., 2016) and first noticed in pressure data by Barnes (1980) in Viking surface pressure data. The strongest waves have periods of ~2 hours, but the wavelet analysis also shows substantial power in periods

shorter than 1 hour. These short-period waves are occurring within a single REMS extended block and the wavelet analysis is ideal for identifying such waves. Some modest wavelet power is present at longer periods, typically associated with single events such as the MY34 global dust storm (see also Figure 12). On a given sol, cumulative wave power can be quite high (>10^5 Pa^2). This cumulative wave power is much higher than suggested by the harmonic analysis, largely because the wavelet analysis is better able to capture transitory, higher-frequency/shorter-period wave activity. However, as shown in Figure 5, the power in a single wavelet packet is typically much more modest (10-40 Pa^2).

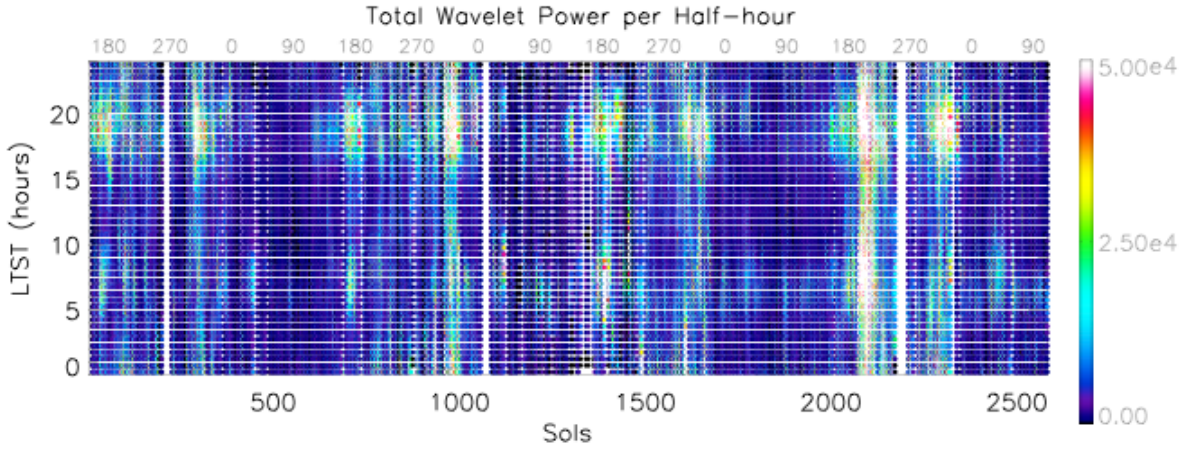

Figure 9. Total wavelet power (Pa^2) per half-hour for the first 2580 sols of the MSL mission as a function of LTST. Times are displayed as centered values in 1/2-hour intervals (e.g., 0015 LTST covers times from 0000-0030 hours).

Figure 9 presents the same data as in Figure 8, but instead shows wavelet power as a function of LTST so that the daily pattern of wave activity can be discerned. The pattern shown in Figure 9 is very similar to that in Figure 6 which showed the standard deviation of the pressure from the tidal harmonic fitting. Wavelet power is predominantly present in the late evening near 2000 LTST, with a weaker period of activity in the morning centered near 0800 LTST. The "quiet" period that was apparent in Figures 6 and 7 is less apparent in the wavelet analysis shown in Figure 9. The same seasonal cycle discussed previously is also distinct, but Figure 9 more

clearly shows isolated events of higher wave activity in the southern hemisphere autumn and winter period (L_s ~ 0-150°). The abnormally large early season dust storm in MY35 at Ls~37° (just before Sol 2500; Malin et al., 2019) shows up clearly with unseasonably high morning wavelet power. This briefly enhanced wavelet power has analogues at very similar times of year in MY 32 and 34 (MY33 had frequent data drop-outs at that time), but with weaker power values, and also with no response in the late evening as is typically seen in the dusty season.

We focus on the strongest wavelets present on each sol of the mission in Figure 10. On certain sols during the dusty season each year, maximum wavelet power exceeds 100 Pa^2, and sometimes reaches 500 Pa^2. For comparison, this is comparable to a typical semidiurnal pressure tide amplitude in Gale Crater, which is often 10-20 Pa (Haberle et al., 2014; Guzewich et al., 2016). More commonly, maximum wavelet power is <40 Pa^2, and during the southern hemisphere autumn and winter (L_s ~ 0-150°) is often <20 Pa^2.

The most quiescent period of the entire mission occurred near Sol 500 (MY 32 L_s ~ 70°) and that is also seen in Figures 6, 8, and 9. This may be simply due to interannual variability, but also could be a reflection of the changing altitude and position of the Curiosity rover within Gale Crater. Near Sol 500, the rover was still within the crater's trough, which tended to stabilize the meteorological environment in a number of ways. As the mission has progressed, the rover has climbed several hundred meters up Aeolis Mons/Mt. Sharp.

On each sol of the mission, the strongest wavelet has a period <3.2 hours with ~2 hours the most common value (Figure 10, bottom panel). This ~2 hour period is appropriate for inertia-gravity waves. The time of day of the strongest wavelet follows the previously identified pattern of evening and early morning preference, with rarer occurrence in the midday hours when the Sun is high in the sky.

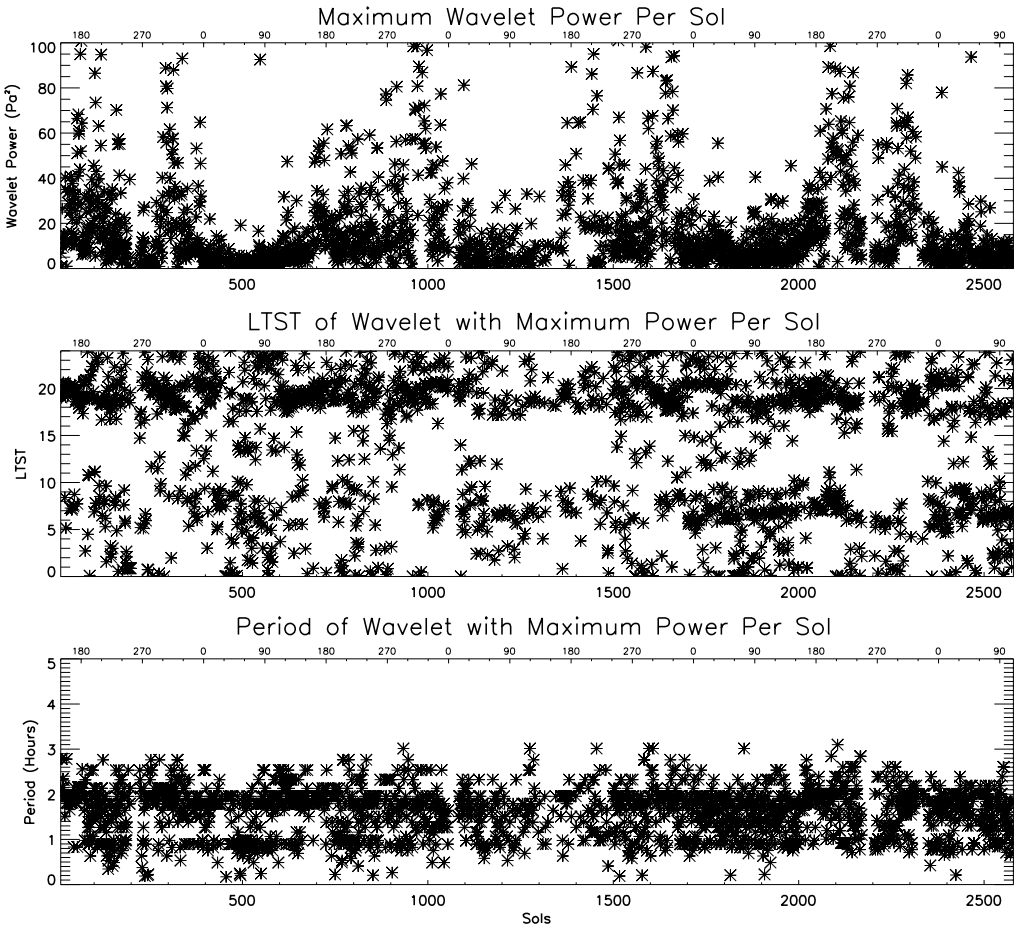

Figure 10. Maximum wavelet power (Pa^2) per sol for the first 2580 sols of the MSL mission (top panel), the LTST of the wavelet with maximum power per sol (middle panel), and the period of the wavelet with maximum power per sol (bottom panel).

During the MY34 global dust storm, the REMS extended block cadence was doubled, leading to a 1-hour duration extended block every 3 hours versus every 6 hours under nominal operations (e.g., Newman et al., 2017; Guzewich et al., 2019). This change was implemented on Sol 2075 and Sol 2075 shows substantially higher wavelet power than Sol 2074 (Figure 11). Still, some of that change is also likely attributable to meteorological effects. The enhanced REMS cadence was continued through Sol 2164 and wave power did decline well before the

REMS cadence returned to nominal (Figure 11). The REMS cadence was also doubled for the late MY34 regional dust storm observed by InSight soon after landing (Banfield and Spiga et al., 2020; Viúdez-Moreiras et al., 2020), but produced a far less abrupt change in wavelet power over the duration of the doubled-cadence (Sols 2291-2306). Wavelet power increased starting on Sol 2285 and then began to weaken again on Sol 2296 (not shown). These examples suggest that if REMS were able to operate at all times a broader mix of wave periods and amplitudes might be detected. Actual changes in the meteorological conditions clearly still drive most of the variations in observed wave properties, however. This is relevant for considering the possible observation cadences of the Mars Environmental Dynamics Analyzer onboard the Mars 2020 Perseverance rover [Rodriguez-Manfredi et al., 2021].

The effect of the rotating REMS extended block cadence can be seen clearly in Figure 11, particularly in the morning near 0800 LTST. When long-duration (2-3 hours or more) extended blocks were scheduled in the ~0600-1000 LTST timeframe, the wavelet analysis measures high wavelet power whereas the wavelet power is weaker on sols with reduced numbers of observations in that timeframe. This effect can be seen in the analysis of data collected according to the nominal REMS cadence before the dust storm campaign was initiated on Sol 2075, in which higher wavelet power is seen in the morning and evening on sols when REMS extended blocks observe those times. Nevertheless, since the REMS extended block cadence rotates through all local times (e.g., Newman et al., 2017), the true meteorological pattern of pressure wave activity can still be seen in Figure 11.

The MY34 GDS clearly strengthened wave activity at all times of day, with a focus on the strongest waves in the morning. We note that this is contrary to what Heavens et al. [2020] and Kuroda et al. [2020] report regarding middle atmospheric gravity wave activity in observed

418 temperatures and in modeling, respectively; however, the strengthening of waves at the surface is
419 consistent with the higher static stability during dusty periods. Upper atmospheric gravity waves
420 were also enhanced during the storm, suggesting a complex altitude-dependent response
421 [Leelavathi et al., 2020]. Wavelet power increased by an order of magnitude from before the
422 storm. During the MY34 GDS, the column opacity peaked on Sol 2085 and then steadily
423 declined afterwards (figure 1 in Guzewich et al., 2019), however the amount of dust measured
424 between MSL and the crater rim (i.e., the amount of dust within the crater rather than above it)
425 had a double-peaked structure with a secondary peak around Sol 2125 (Smith et al., 2019;
426 Lemmon et al., 2019). The wave response more closely follows the pattern of the column
427 opacity, particularly for the waves in the evening, with a peak soon after the storm arrived in
428 Gale Crater and then a long tail toward Sol 2160 as the storm decayed.

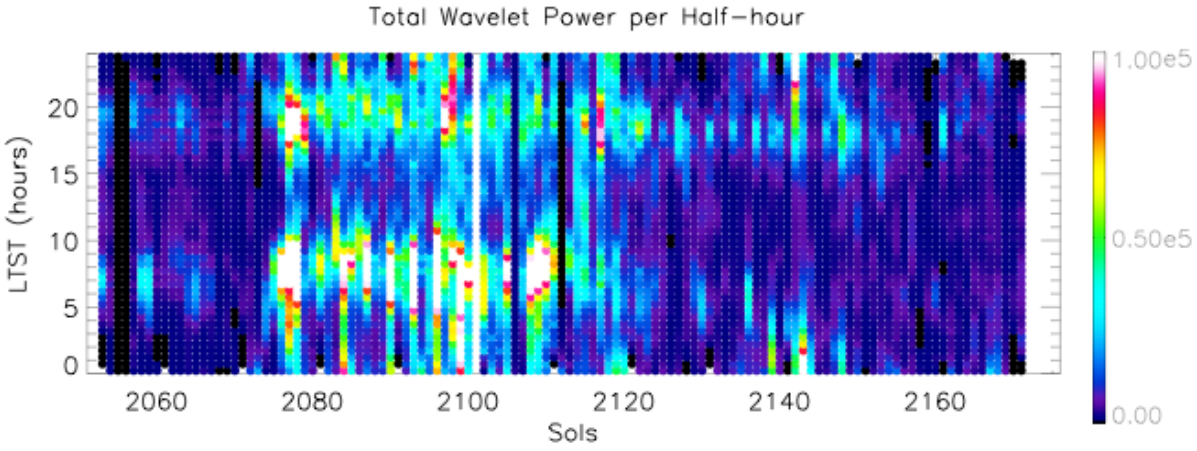

429

430 Figure 11. Total wavelet power (Pa^2) per sol for Sols 2050-2175 of the MSL mission, focused
431 on the MY34 global dust storm, as a function of LTST. Times are displayed as centered values
432 in 1/2-hour intervals (e.g., 0015 LTST covers times from 0000-0030 hours).
433

434

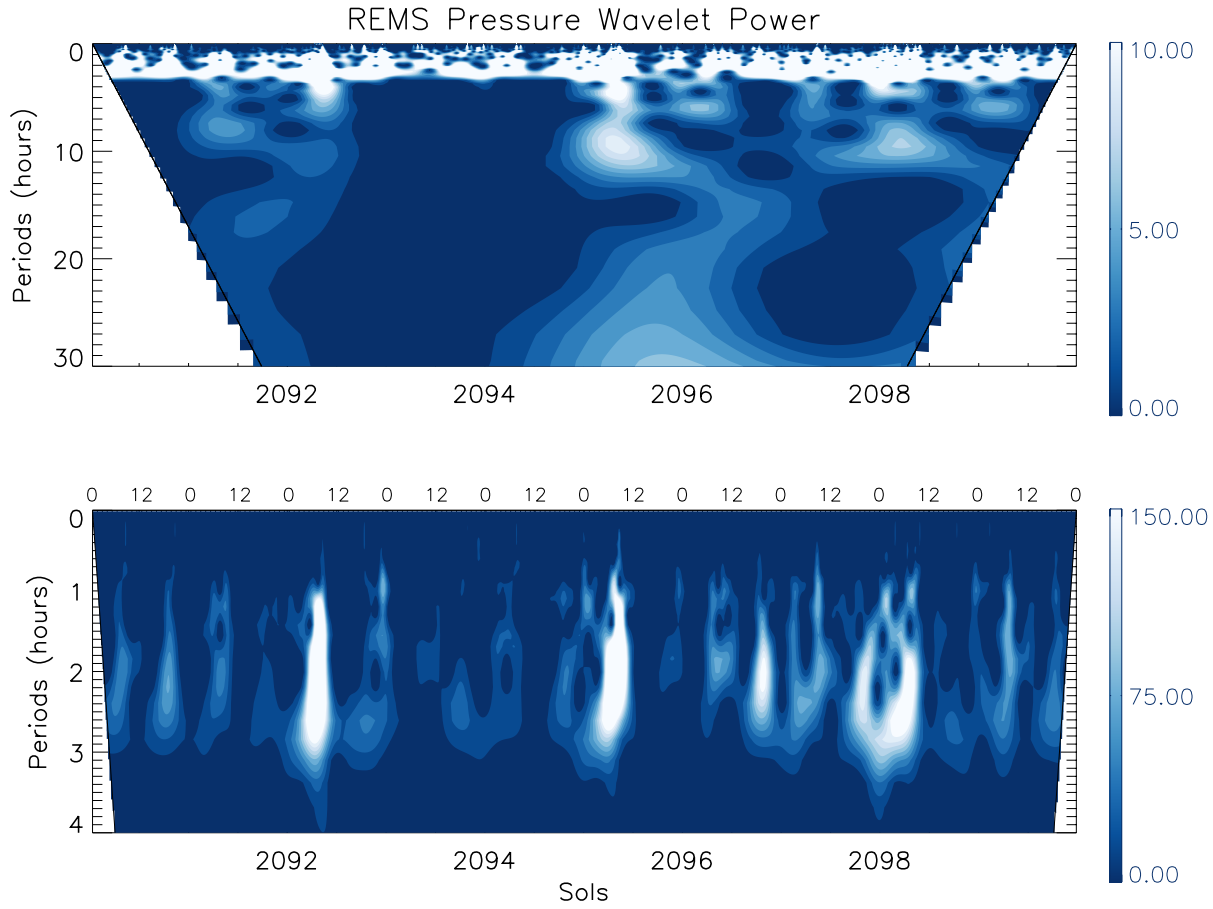

Figure 12. REMS pressure wavelet power (Pa^2) for the Sol 2090-2099 period during the MY34 global dust storm. The bottom panel is zoomed in to highlight periods less than 4 hours and local time is labeled on the top abscissa for reference. The cone of influence is represented by the thick black diagonal lines in each panel. Notice the different color bars for each panel.

Figure 12 shows the wavelet spectrum at the peak of the storm (as delineated by dust opacity). Unlike almost any other time period in the entire mission, there is non-negligible wavelet power at long periods. Sol 2095, in particular, exhibits wavelet power with periods of ~9-10 hours and then an additional region of wavelet power of periods >20 hours. As discussed in Section 2, our choice of 8 harmonics (essentially filtering wave periods longer than 3 hours) likely weakens the depicted power at these long wave periods relative to reality. Note that periods > ~12 hours (lower frequency than the inertial frequency at Gale Crater) are not inertia-

449 gravity waves, by definition. The bottom panel of Figure 12 focuses on the periods <4 hours.
450 The every-3-sol repeat pattern of the cadence is seen in the morning peaks of wavelet power on
451 Sols 2092, 2095, and 2098. The peak wavelet power occurs with periods of 2-3 hours.
452
453 3.3. MarsWRF Results
454 The MarsWRF GCM simulations allow us to have complete and consistent local time
455 coverage of each sol and the ability to study wave behavior at different locations near Gale
456 Crater and Elysium Planitia. Ultimately, this helps us interpret the REMS observations, as
457 single-station observations have inherent biases and limitations and can provide us with no
458 information about the cause or source of the waves detected by REMS.
459 To more directly compare with the REMS analysis, we perform wavelet analysis on the
460 MarsWRF surface pressure values at the model grid point nearest to Curiosity's landing site. As
461 stated in Section 2.2, we are using Domain 3 of the simulations defined by Newman et al. (2017)
462 which have a horizontal spatial resolution of ~13 km. Figure 13 is designed to be directly
463 compared with Figure 10, which provides an overview of wavelet analysis of the REMS pressure
464 observations.

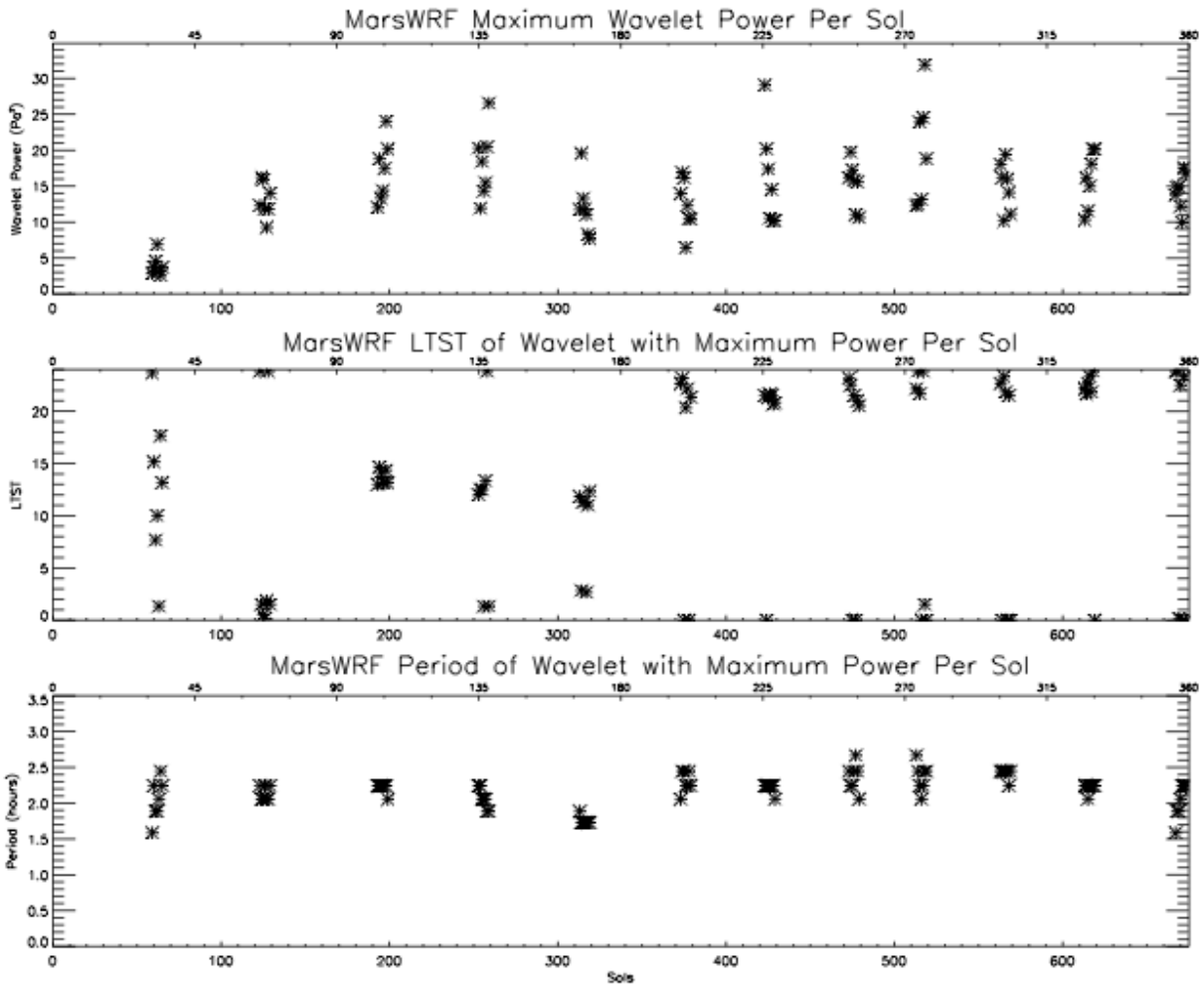

Figure 13. Maximum wavelet power (Pa^2) per sol for each MarsWRF simulation (top panel), the LTST of the wavelet with maximum power per sol (middle panel), and the period of the wavelet with maximum power per sol (bottom panel).

Like the REMS observations, MarsWRF finds that the strongest wavelets on a given sol typically have periods near 1.5-2.5 hours, with very slight seasonal variations. However, MarsWRF simulates weaker waves relative to observations, with maximum wavelet power of 10-30 Pa^2, which is a factor of 2-3 weaker than REMS observations. REMS observations also exhibited a strong seasonal cycle in maximum wavelet power, with a minimum near $L_s = 90°$ (Figure 10). MarsWRF does show distinctly weaker waves near $L_s = 30°$, but the remainder of

476 the year sees minimal variation (Figure 13). The local time of the strongest wave each sol is
477 clustered around midnight (2100-0100 LTST) during the second half of the year (L_s = 180°-
478 360°), while the first half of the year often shows midday (~1200 LTST) occurrences as well.
479 This shows some broad agreement with the REMS observations, where the first half of the year
480 (L_s = 0°-180°) also has the strongest wave occur during midday occasionally. However, the
481 frequent clustering near 1800-2100 LTST and again near ~0700 LTST seen in REMS
482 observations is entirely absent from the simulations. In brief, the MarsWRF simulations
483 underestimate the strength of these non-tidal waves, but corroborate the period and some aspects
484 of the diurnal timing of the waves. Of course, we cannot be sure that the waves in REMS
485 observations are produced by the same physical mechanism as these broadly similar waves in the
486 MarsWRF simulations. But we make that reasonable assumption to try and help guide us to
487 understanding those mechanism/s.

488 Integrating over all wavelets with periods under four hours leads us to Figure 14. Figure
489 14 can be directly compared to Figure 8, which shows the comparable values from the REMS
490 observations. Of particular note are the different scales, with the MarsWRF total wavelet power
491 substantially less (by a factor of 10 or more) than that seen in the REMS observations. This
492 trend of weaker simulated waves can also be seen in Figure 13, showing the same behavior for
493 the strongest wavelet on a given sol. Guzewich et al. [2016] presented a similar situation where
494 MarsWRF simulations underestimated atmospheric tide amplitudes in surface pressure, likely
495 due to the difference between the dust opacity used in the model vs. reality and insufficient
496 spatial resolution. We have no unique explanation for why the simulated waves are consistently
497 weaker, but can suggest a couple of possibilities. Our MarsWRF simulations use a simple, and
498 modest, atmospheric dust opacity climatology. As seen in Figure 11, the higher dust loading in

499 reality on Mars leads to stronger waves and dustier conditions, likely explaining some of the
500 discrepancy. The difference in observation cadence and model output frequency may play a role
501 as well. As shown in Figure 3, the REMS observation cadence creates "leakage" of amplitude to
502 periods other than the true period, but in our idealized experiments this reduces rather than
503 increases the total wavelet amplitude. The MarsWRF model's consistent output rate (every 10
504 minutes across all nine sols) should prevent aliasing between periods from occurring, but the net
505 effect of the discrepancy between observation and model is difficult to directly quantify. Lastly,
506 the model may simply lack sufficient resolution or physics to properly simulate these waves.
507 The simulations do corroborate the observations in the wave periods with the highest
508 amplitudes, 1-3 hours. MarsWRF, however, underestimates the wave amplitudes in the shortest
509 waves and the seasonal cycle is muted relative to the REMS observations. The discrepancy at
510 the shortest periods is easier to understand as a cause of the difference between REMS
511 observation cadences and model output frequency. REMS extended blocks allow waves with
512 periods under 1 hour to be fully resolved (although background 5 minute hourly observations do
513 not), relative to 10 minute output frequency in the model. At the MarsWRF resolution, short-
514 duration fluctuations at high frequencies will be smoothed, which partially drove our selection of
515 a 10 minute output frequency. Coupled with the horizontal resolution of the model simulations,
516 which may mask wave forcing mechanisms that drive higher frequency/shorter period waves
517 (see Section 4), we believe this likely explains the relative lack of short period waves in the
518 model relative to REMS observations.

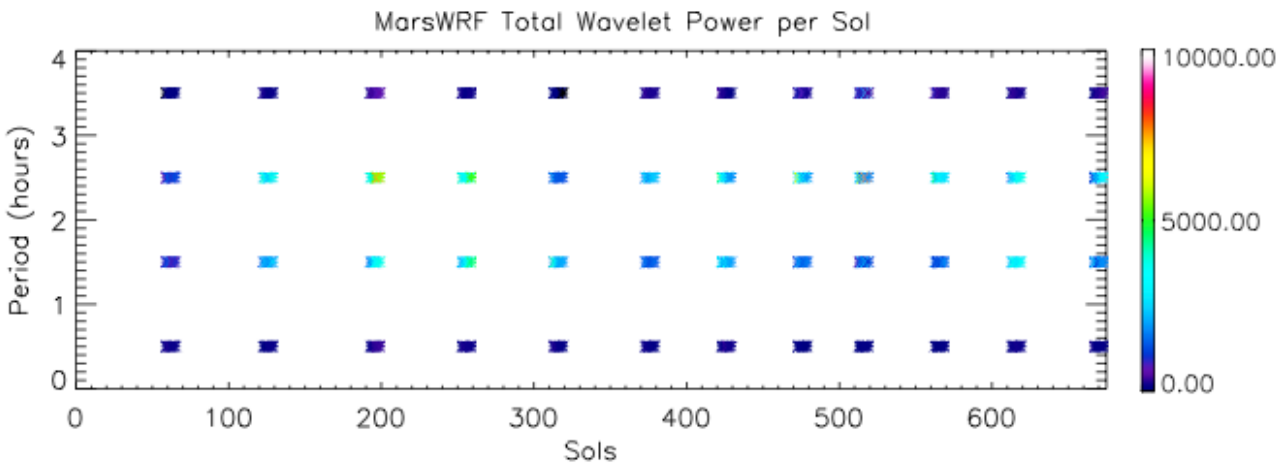

519

520 Figure 14. Total wavelet power (Pa^2) per sol for each MarsWRF simulation as a function of
521 period (hours). Periods are displayed as centered values in 1-hour intervals (e.g., 0.5 hour period
522 covers periods from 0-1 hour).
523
524 Most importantly, MarsWRF can help guide us to the source of these waves. To this
525 point, we have not discussed the physical mechanism that is producing waves with periods under
526 4 hours in surface pressure in Gale Crater. Our assumption is that these are inertia-gravity waves
527 due to their amplitudes and periods, but we can not produce any genetic connection between
528 REMS pressure variations and the physical mechanism producing them (be it air flow over
529 topography, jets, fronts, or something else) with the observations alone. The spatial information
530 provided by the model allows us to determine the direction in which these waves are
531 propagating. We employ an array analysis method that has its heritage in terrestrial seismology
532 and is described in detail by Hedlin et al. [2018] (and references therein). In brief, the method
533 works by examining three stations (in our case, three model grid points) and looking at the cross-
534 correlation and lag between the pressure perturbations caused by a passing wave at each station.
535 From this, the phase speed and azimuth of the wave can be determined. In our MarsWRF
536 simulations, we use a variety of grid points, in addition to the grid point nearest the MSL landing

site in Gale Crater, to more robustly determine the phase speed and azimuths of the waves present in the simulations.

Figure 15 presents the results from this array analysis to identify the predominant wave azimuths and phase speeds present in the MarsWRF simulations. In all seasons, we present the two most common wave azimuths and their associated phase speeds. There is very little seasonal variation to the wave azimuths, with the majority of the waves coming from the north (352-360°) and the second most common azimuth of south-southeast, south, or south-southwest (163-188°). The standard deviations of those azimuths are shown in Figure 15 as error bars and are approximately 20-25° for most seasons. As Gale Crater sits on the topographic dichotomy boundary, these directions make sense with the assumption that these are largely topographically-driven waves. Strong jet streams or other dynamic conditions that could generate inertia-gravity waves are far from Gale Crater (typically poleward of 45° latitude). Elysium Mons is to the north and north-northeast of Gale, while the rugged terrain of the southern highlands of Terra Cimmeria is to the south. Regional analysis of the MarsWRF simulations shows Elysium Mons produces widespread and frequent gravity and inertia-gravity wave activity that propagates through the entire high spatial resolution domains and likely beyond. Waves could also be produced nearer to the Curiosity rover by the crater rim or Aeolis Mons (e.g., Rafkin et al., 2016), however we expect those to have much shorter horizontal wavelengths and shorter periods/higher frequency [Harri et al., 2014; Haberle et al., 2014; Ullán et al., 2017] than the longer wavelength waves with periods of tens of minutes to hours that we focus on. That may explain the relative lack of wavelet power with wave periods <1 hour in the MarsWRF analysis relative to REMS observations.

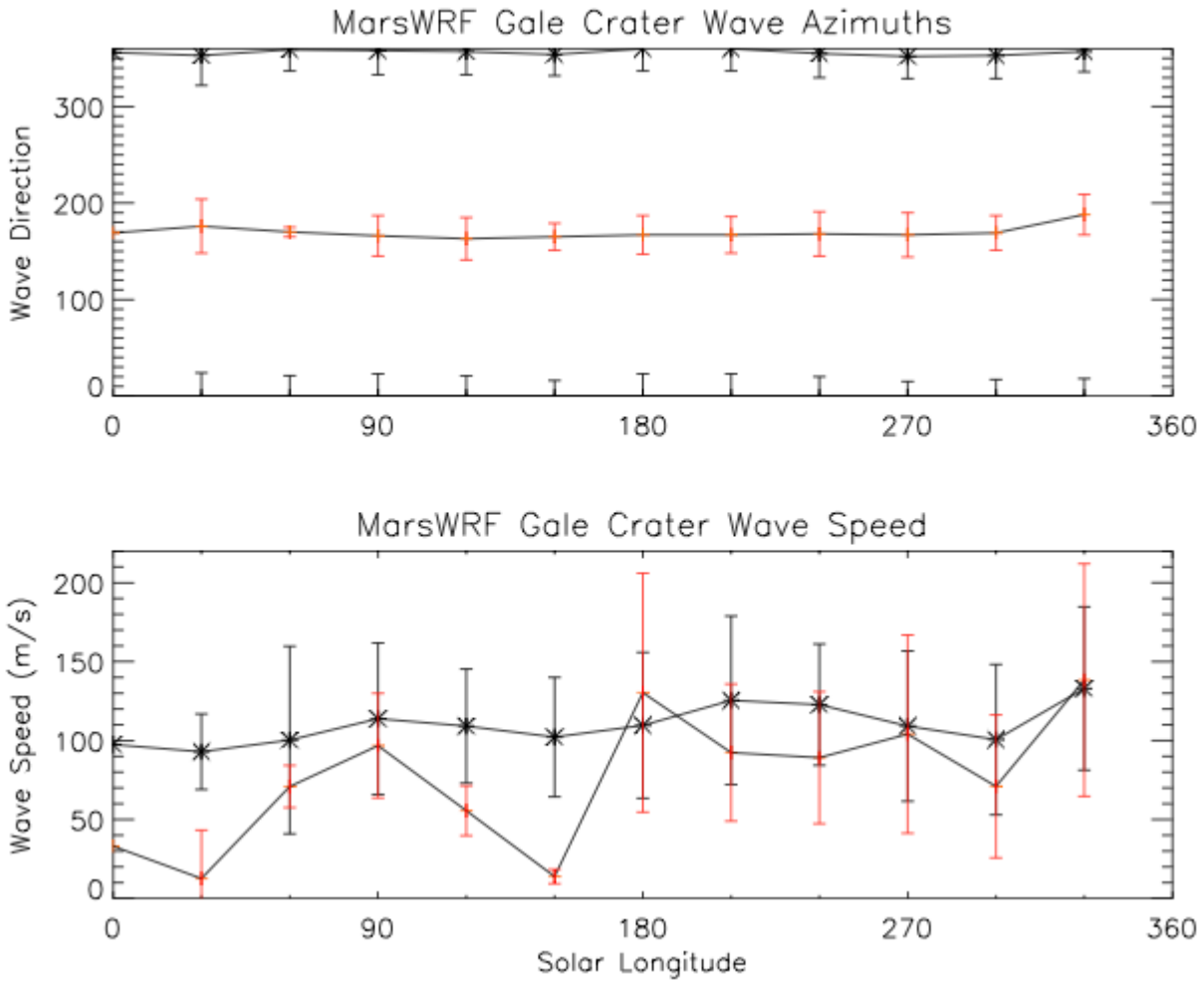

Figure 15. Predominant daily average MarsWRF pressure wave azimuths (top) and phase speeds (m/s, bottom). Black asterisks show waves propagating from a northerly direction while red crosses indicate those propagating from a southerly direction. One standard deviation around each value is shown as error bars.

The phase speeds shown in Figure 15 also aid in determining the type of waves we have identified in the simulations, and by analogy, in REMS observations. Migrating atmospheric tides, by definition, have phase speeds that are equal to the linear rotation speed of Mars: 241 m/s at the equator. Figure 15 shows that the detected wave phase speeds are well below that value and thus are not migrating tides with periods of 2 or 3 hours. These phase speeds, coupled with predominant periods of 1-3 hours, imply horizontal wavelengths of ~200-1500 km under the shallow water assumption. These values are directly comparable to those seen in Earth's

573 stratosphere and mesosphere for atmospheric gravity waves (e.g, Ern et al., 2018). Additionally,
574 shallow water theory implies that the phase speed is equal to $\sqrt{gh}$ where g is gravitational
575 acceleration and h is the "equivalent depth." Using Mars' gravitational acceleration and the
576 phase speeds shown in Figure 15, we calculate typical equivalent depths of 600 m - 6 km. These
577 values are comparable to typical daytime atmospheric boundary layer depths in Gale Crater
578 [Tyler and Barnes, 2015; Guzewich et al., 2017].
579
580 4. DISCUSSION AND CONCLUSIONS
581 We have searched for non-tidal pressure and temperature perturbations with periods of
582 tens of minutes to hours in REMS observations using harmonic fitting and wavelet analysis.
583 Analysis of REMS temperature observations are consistent with daytime convective turbulence
584 and show no coherent non-tidal patterns with longer periods. Detailed analysis of this turbulence
585 is reserved for future work. On the other hand, REMS pressure observations, after removing the
586 atmospheric tides, do show coherent wave-like behavior with such periods using wavelet
587 analysis. Our methods bias our detections to wave periods less than 3 hours, but occasionally
588 longer-period waves were seen.
589 We find that such waves typically have amplitudes of O(1-10 Pa) and have a distinct
590 diurnal and seasonal cycle. Waves are most clearly present in the evening (1700-2400 LTST)
591 and early morning (0400-0800 LTST) with a distinct "quiet" period near sunset that was also
592 recently identified by InSight [Banfield and Spiga et al., 2020]. Pressure wave activity detected
593 by REMS is strongest in the southern spring and summer seasons (L_s = 180-330°) with a local
594 minimum in activity near southern summer solstice (L_s = 270°), analogous to the solsticial pause
595 seen in dust storm and baroclinic wave activity across the planet (e.g., Barnes, 1980; Lewis et al.,
596 2016). The MY34 global dust storm saw the strongest activity of the entire mission with some

597 waves having amplitudes comparable to migrating atmospheric tides (e.g., Guzewich et al.,
598 2016).

599 To augment and complement the REMS data analysis, we conducted a series of high
600 spatial resolution atmospheric simulations with the MarsWRF GCM. The simulations generally
601 corroborate the patterns seen in REMS observations in terms of predominant wave periods and
602 the diurnal cycle of wave activity. However, the simulations produce wave amplitudes (or
603 power) that are typically a factor of 2-5 weaker and don't replicate the seasonal cycle seen by
604 REMS. This may be due to the prescribed dust climatology in the MarsWRF simulations. The
605 ability to simulate the entire region gives us additional information on how such waves may be
606 generated, their sources, and additional wave properties that are unknowable from a single
607 meteorological station on the surface of Mars. Analysis of the wave azimuths and phase speeds
608 in the simulations clearly show these are non-tidal waves with phase speeds and wavelengths that
609 are directly comparable to terrestrial atmospheric gravity waves, particularly those detected in
610 the terrestrial stratosphere and mesosphere.

611 We note that short-period (<1 hour) wavelet power is one particular area of discrepancy
612 between the REMS observations and the mesoscale modeling with the GCM. As mentioned in
613 Section 3.3, this is plausibly due to the model's spatial resolution not fully capturing wave
614 activity (and associated forcing mechanisms) that occur at scales near or below the model's
615 resolution. Here we postulate a forcing mechanism for such short-period waves based on
616 terrestrial mountain meteorology and suggest that the short period waves poorly resolved in the
617 GCM may be produced through a different forcing mechanism than the longer period waves that
618 are simulated in MarsWRF.

The northwest slope of Aeolis Mons / Mt. Sharp and the walls of Gale Crater form a ~13 km wide valley (comparable to the spatial resolution of the MarsWRF nested domain) around the study area of Curiosity, oriented WSW to ENE. The phase speed calculated in the GCM is consistent with an equivalent depth of 600 m-6 km which is comparable to the extent of the boundary layer and possibly the inversion layer. Therefore, an analogy to the mechanisms that might be occurring is found in terrestrial mountain meteorology, starting with the scheme found by Defant (1949). As the Sun sets, Gale's northern wall starts casting shadow on its own slope, thus cooling down radiatively at a time when Aeolis Mons remains illuminated. Cold air near the surface of the northern crater wall sinks into the valley and this downslope jet generates shear that can cause internal gravity waves with some backlash as the jet reaches the southern wall and bounces back. This would happen in the evening before sunset, thus explaining the standard deviation increase near 1700 LTST (Figure 6). After sunset as a stable inverse thermal layer develops and grows in altitude, winds cannot reach the bottom of the crater and a shear layer forms above the surface (e.g. Whiteman, 2000; Sun et al., 2001). The lower altitudes remain subject to the echo of these higher altitude waves that are much stronger seasonally when higher altitude winds are stronger. During the dust season, high altitude winds strengthen and the vertical temperature gradients decrease thus weakening the thermal inversion. A weaker thermal inversion between 2000 and 0500 LTST results in lower static stability and higher sensitivity to perturbations from activity/turbulence by the higher altitude winds in the dust season. In the morning as the Sun rises, the nighttime inversion breaks up with the start of convection seen in the ~0800 LTST temperature fluctuations. The volume of air trapped in the crater is smaller and therefore heats up faster than the plains around the crater, thus producing an outflow of air from the bottom of the crater up the slopes and a subsidence of air into the center of the crater. This

642 flow is also coupled with a crater internal circulation along the crater bottom as the sun-facing
643 west side of the crater starts warming up radiatively at a time when the west slopes of Aeolis
644 Mons are still shaded and remain colder. This horizontal temperature gradient east to west will
645 generate a background wind oriented nearly 90° to the upslope winds, thus creating a wind shear
646 in the morning until the east-west temperature difference has been compensated well after LTST
647 sunrise (~0700), contemporary with the morning pressure fluctuations and the temperature
648 fluctuations in Figure 9 at 0700-0800 LTST. Because of their origin, the morning short-period
649 fluctuations are a radiation-driven effect related to the direction of the solar radiation. The effect
650 should be stronger under clear skies, and decrease when atmospheric dust homogenizes the light
651 resulting in smaller east-west radiative heating differences. It is interesting that the opposite
652 effect is observed on pressure where Figure 9 shows it to be strongest right before and after the
653 dust season.

654 In combination, we interpret the waves (particularly those with periods >1 hour) detected
655 by REMS to be inertia-gravity waves. The wavelengths calculated in the model (~200-1500 km)
656 imply that these longer-period waves are likely not produced locally within Gale Crater, but
657 farther afield in the southern hemisphere highlands or from Elysium Mons and its associated
658 high terrain, which suggests these waves may be topographically-forced. Dynamically-forced
659 inertia-gravity waves (e.g., near jet streams) are also possible and the reduction in inertia-gravity
660 wave activity near southern summer solstice may point toward such a source. Our work, in
661 conjunction with that from InSight (e.g., Banfield and Spiga, et al., 2020), help extend
662 understanding of martian atmospheric gravity and inertia-gravity waves to the surface. Previous
663 model studies (Forget et al., 1999; Kuroda et al., 2015; Gilli et al., 2019) and analysis of orbital
664 datasets (e.g., Heavens et al., 2020) have largely focused on the substantial impact that breaking

gravity waves have on the atmospheric temperature structure and circulation in the middle and upper atmosphere. Here we show that they are clearly detectable with surface pressure stations, while not being seen in surface temperature observations (at least not those taken with the frequency and cadence of REMS). Our work further fills in the phase space of martian atmospheric phenomena, which extends from convective vortices with durations of seconds, to atmospheric tides with periods of hours that are integer fractions of a solar day, to baroclinic and barotropic waves with periods of days, and to the sublimation and deposition of the polar caps with a period of a Martian year.

ACKNOWLEDGMENTS

Guzewich, Smith, and Khayat were supported by the MSL Participating Scientist program. de la Torre Juarez, Newman, Kahanpää, Viúdez-Moreiras, and Richardson were supported by the REMS instrument. Mason was supported by the NASA Postdoctoral Program, administered by the Universities Space Research Association. REMS pressure and temperature data are freely available on the Planetary Data System (https://atmos.nmsu.edu/PDS/data/mslrem_1001/). MarsWRF simulation output and derived REMS data used to make figures is available at Guzewich et al. (2021).

REFERENCES

Altieri, F., Spiga, A., Zasova, L., Bellucci, G., and Bibring, J.-P. (2012), Gravity waves mapped by the OMEGA/MEX instrument through O_2 dayglow at 1.27 μm: Data analysis and atmospheric modeling, *J. Geophys. Res.*, 117, E00J08, doi:10.1029/2012JE004065.

Banfield, D., Spiga, A., Newman, C. *et al.* (2020), The atmosphere of Mars as observed by InSight, *Nat. Geosci.* 13, 190–198, https://doi.org/10.1038/s41561-020-0534-0

Barnes, J. R. (1980). Time spectral analysis of midlatitude disturbances and chaos in a fractal basin boundary regime of a Josephson Junction. in the martian atmosphere. J. Atmos. Sci. 37, 2002–2015.

Blanc, E., Farges, T., Le Pichon, A., and Heinrich, P. (2014), Ten year observations of gravity waves from thunderstorms in western Africa, *J. Geophys. Res. Atmos.*, 119, 6409– 6418, doi:10.1002/2013JD020499.

Bretherton, F. P. (1966), The propagation of groups of internal gravity waves in a shear flow.*Quart. J. Roy. Meteor. Soc*, **92 ,** 466–480.

Calderón, A.P. (1964), Intermediate spaces and interpolation, the complex method. *Studia Math*. **24**, 113–190.

Clinton, J.F., S. Ceylan, M. van Driel, D. Giardini, S.C. Stähler, M. Böse, C. Charalambous, N.L. Dahmen, A. Horleston, T. Kawamura, A. Khan, G. Orhand-Mainsant, J.-R. Scholz, F. Euchner, W.B. Banerdt, P. Lognonné, D. Banfield, E. Beucler, R.F. Garcia, S. Kedar, M.P. Panning, C. Perrin, W.T. Pike, S.E. Smrekar, A. Spiga, and A.E. Scott (2021), The Marsquake catalogue from InSight, sols 0-478, Physics of Earth and Planetary Interiors, 310, 106595, https://doi.org/10.1016/j.pepi.2020.106595.

Collins M., S.R. Lewis, P.L. Read, and F. Hourdin (1996), Baroclinic Wave Transitions in the Martian Atmosphere, Icarus, no.2, 344-357.

Creasey, J. E., Forbes, J. M., and Hinson, D. P. (2006), Global and seasonal distribution of gravity wave activity in Mars' lower atmosphere derived from MGS radio occultation data, *Geophys. Res. Lett.*, 33, L01803, doi:10.1029/2005GL024037.

Defant, F., (1949). Zur Theorie der Hangwinde, nebst Bemerkungen zur Theorie der Berg- und Talwinde (A theory of slope winds, along with remarks on the theory of mountain winds and valley winds). *Arch. Meteor. Geophys. Bioklimatol.*, **1A ,** 421–450.

Gossard, E., & Munk, W. (1954). On Gravity Waves in the Atmosphere, *Journal of Atmospheric Sciences*, *11*(4), 259-269, https://doi.org/10.1175/1520-0469(1954)011<0259:OGWITA>2.0.CO;2

Guzewich, S.D., Newman, C.E., de la Torre Juárez, M., Wilson, R.J., Lemmon, M., Smith, M.D., Kahanpää, H., Harri, A.-M., the REMS Science Team, and the MSL Science Team (2016). Atmospheric Tides in Gale Crater, Mars. Icarus, 268, 37-49, https://doi.org/10.1016/j.icarus.2015.12.028.

Guzewich, S. D., Newman, C. E., Smith, M. D., Moores, J. E., Smith, C. L., Moore, C., … Battalio, M. (2017). The vertical dust profile over Gale Crater, Mars. *Journal of Geophysical Research: Planets*, 122, 2779– 2792. https://doi.org/10.1002/2017JE005420

Guzewich, S. D., Lemmon, M., Smith, C. L., Martínez, G., de Vicente-Retortillo, Á., Newman, C. E., et al. (2019). Mars Science Laboratory observations of the 2018/Mars year 34 global dust storm. *Geophysical Research Letters*, 46, 71– 79. https://doi.org/10.1029/2018GL080839

Guzewich, S.D., M. de la Torre Juarez, C.E. Newman, E. Mason, M.D. Smith, N. Miller, A.S.J. Khayat, H. Kahanpää, D. Viúdez-Moreiras, M.I. Richardson (2021), Gravity Wave Observations by the Mars Science Laboratory REMS Pressure Sensor and Comparison with Mesoscale Atmospheric Modeling with MarsWRF, https://doi.org/ 10.5281/zenodo.4926323.

Haar, A. (1910), *Zur Theorie der orthogonalen Funktionensysteme*, Mathematische Annalen, **69**, pp 331–371.

742 Haberle, R. M., et al. (2014), Preliminary interpretation of the REMS pressure data from the first
743 100 sols of the MSL mission, *J. Geophys. Res. Planets*, 119, 440– 453,
744 doi:10.1002/2013JE004488.

745 Haberle, R.M., M. de la Torre Juárez, M.A. Kahre, D.M. Kass, J.R. Barnes, J.L. Hollingsworth,
746 A.-M. Harri, and H. Kahanpää (2018), Detection of Northern Hemisphere transient eddies at
747 Gale Crater Mars, *Icarus*, 307:150-160, doi:10.1016/j.icarus.2018.02.013.

748 Harri, A.-M., et al. (2014), Pressure observations by the Curiosity rover: Initial results, *J.*
749 *Geophys. Res. Planets*, 119, 82– 92, doi:10.1002/2013JE004423.

750 Heavens, N.G., D.M. Kass, A. Kleinböhl, and J.T. Schofield (2020), A multiannual record of
751 gravity wave activity in Mars's lower atmosphere from on-planet observations by the Mars
752 Climate Sounder, Icarus, 341(1), 113630, https://doi.org/10.1016/j.icarus.2020.113630.

753 Hedlin, M. A. H., de Groot-Hedlin, C. D., Forbes, J. M., & Drob, D. P. (2018). Solar
754 terminator waves in surface pressure observations. *Geophysical Research Letters*, 45, 5213–
755 5219. https://doi.org/10.1029/2018GL078528
756
757 Hourdin, F. P. Le Van, F. Forget, O. Talagrand, Meteorological variability and the annual
758 surface pressure cycle on Mars (1993), J. Atmos. Sci. 50(21), 3625–3640.
759
760 Kahanpää, H., et al. (2016). Convective vortices and dust devils at the MSL landing site: Annual
761 variability. *J. Geophys. Res. Planets*, 121, 1514– 1549. https://doi.org/10.1002/2016JE005027
762
763 Kahanpää, H., and D. Viúdez-Moreiras (2021). Modelling Martian dust devils using in-situ wind,
764 pressure, and UV radiation measurements by Mars Science Laboratory. *Icarus*, 359, 114207.
765 https://doi.org/10.1016/j.icarus.2020.114207

766 Kloos, J.L., J.E. Moores, J.A. Whiteway, and M. Aggarwa (2018)l, Interannual and diurnal
767 variability in water ice clouds observed from MSL over two Martian years, *Journal of*
768 *Geophysical Research Planets*, 123(1):233- 245, doi:10.1002/2017JE005314.

769 Kuroda, T., Medvedev, A. S., Yiğit, E., and Hartogh, P. (2015), A global view of gravity
770 waves in the Martian atmosphere inferred from a high-resolution general circulation model,
771 *Geophys. Res. Lett.*, 42, 9213– 9222, doi:10.1002/2015GL066332.
772
773 Kuroda, T., Yiğit, E., & Medvedev, A. S. (2019). Annual cycle of gravity wave activity
774 derived from a high-resolution Martian general circulation model. *Journal of Geophysical*
775 *Research: Planets*, 124, 1618– 1632. https://doi.org/10.1029/2018JE005847
776
777 Kuroda, T., Medvedev, A. S., & Yiğit, E. (2020). Gravity wave activity in the atmosphere of
778 Mars during the 2018 global dust storm: Simulations with a high-resolution model. *Journal of*
779 *Geophysical Research: Planets*, 125 e2020JE006556. https://doi.org/10.1029/2020JE006556
780
781 Leelavathi, V., Venkateswara Rao, N, & Rao, S.V. B.. (2020). Inter-annual variability of
782 atmospheric gravity waves in the martian thermosphere: Effects of the 2018 planet-encircling

783 dust event. *Journal of Geophysical Research: Planets*, 125, e2020JE006649.
784 https://doi.org/10.1029/2020JE006649
785
786 Lemmon, M. T., Guzewich, S. D., McConnochie, T., de Vicente-Retortillo, A., Martínez, G.,
787 Smith, M. D., et al. (2019). Large dust aerosol sizes seen during the 2018 Martian global dust
788 event by the Curiosity rover. *Geophysical Research Letters*, 46, 9448– 9456.
789 https://doi.org/10.1029/2019GL084407
790
791 Lewis, S.R., D.P. Mulholland, P.L. Read, L. Montabone, R.J. Wilson, and M.D. Smith (2016),
792 The solsticial pause on Mars: 1. A planetary wave reanalysis, Icarus, 264, 456-464,
793 https://doi.org/10.1016/j.icarus.2015.08.039.
794
795 Magalhães, J. A., Schofield, J. T., and Seiff, A. (1999), Results of the Mars Pathfinder
796 atmospheric structure investigation, *J. Geophys. Res.*, 104(E4), 8943– 8955,
797 doi:10.1029/1998JE900041.
798
799 Malin, M. C., B. A. Cantor, A. W. Britton (2019), MRO MARCI Weather Report for the week of
800 3 June 2019 – 9 June 2019, Malin Space Science Systems Captioned Image Release, MSSS-583,
801 http://www.msss.com/msss_images/2019/06/12/.
802
803 Marlton, G. J., Williams, P. D., & Nicoll, K. A. (2016). On the detection and attribution of
804 gravity waves generated by the 20 March 2015 solar eclipse. *Philosophical transactions. Series*
805 *A, Mathematical, physical, and engineering sciences*, *374*(2077), 20150222.
806 https://doi.org/10.1098/rsta.2015.0222
807
808 Martínez, G.M., Newman, C.N., De Vicente-Retortillo, A. *et al* (2017), The Modern Near-
809 Surface Martian Climate: A Review of In-situ Meteorological Data from Viking to Curiosity.
810 *Space Sci Rev* 212, 295–338, https://doi.org/10.1007/s11214-017-0360-x.
811
812 Mason, E.M., and M.D. Smith (2021) Temperature fluctuations and Boundary Layer Turbulence
813 as seen by Mars Exploration Rovers Miniature Thermal Emission Spectrometer, *Icarus,* 360,
814 114350, https://doi.org/10.1016/j.icarus.2021.114350.
815
816 Miller, N. M., de la Torre Juárez, M., & Tamppari, L. (2018). The effect of Bagnold dunes
817 slopes on the short timescale air temperature fluctuations at Gale crater on Mars. *Geophysical*
818 *Research Letters*, 45, 11,588– 11,594. https://doi.org/10.1029/2018GL080542
819
820 Newman, C. E., Kahanpää, H., Richardson, M. I., Martinez, G. M., Vicente-Retortillo, A., &
821 Lemmon, M. (2019). Convective vortex and dust devil predictions for gale crater over 3 mars
822 years and comparison with MSL-REMS observations. *Journal of Geophysical Research:*
823 *Planets*, 124, 3442– 3468. https://doi.org/10.1029/2019JE006082
824
825 Ordonez-Etxeberria, I., Hueso, R. & Sánchez-Lavega, A (2018), A systematic search of sudden
826 pressure drops on Gale Crater during two Martian years derived from MSL/REMS data, *Icarus*
827 299, 308–330,https://doi.org/10.1016/j.icarus.2020.113814.

828 Ordonez-Etxeberria I., Hueso, R., and Sánchez-Lavega, A. (2020). Strong increase in dust devil
829 activity at Gale crater on the third year of the MSL mission and suppression during the 2018
830 Global Dust Storm. *Icarus*, 347, 113814. https://doi.org/10.1016/j.icarus.2020.113814

831 Plougonven, R., and F. Zhang (2014), Internal gravity waves from atmospheric jets and fronts,
832 *Rev. Geophys.*, *52*, 33–76, doi:10.1002/2012RG000419.

833 Rafkin, S.C.R., J. Pla-Garcia, M. Kahre, J. Gomez-Elvira, V.E. Hamilton, M. Marín, S. Navarro,
834 J. Torres, and A. Vasavada (2016), The meteorology of Gale Crater as determined from Rover
835 Environmental Monitoring Station observations and numerical modeling. Part II: Interpretation,
836 Icarus, 280, 114-138, https://doi.org/10.1016/j.icarus.2016.01.031.
837
838 Rafkin, Scot C. R., Aymeric Spiga, Timothy I. Michaels (2017). Mesoscale Meteorology. In R.
839 Haberle, R. Clancy, F. Forget, M. Smith, & R. Zurek (Eds.), *The Atmosphere and Climate of*
840 *Mars* (Cambridge Planetary *Science*, pp. 172-202). Cambridge: Cambridge University Press.
841 doi:10.1017/9781139060172.007.

842 Richardson, M.I., and C.E. Newman (2018), On the relationship between surface pressure,
843 terrain elevation, and air temperature. Part I: The large diurnal surface pressure range at Gale
844 Crater, Mars and its origin due to lateral hydrostatic adjustment, *Planetary and Space Science*,
845 164:132-157, doi:10.1016/j.pss.2018.07.003.

846 Rodriguez-Manfredi, J.A. et al. (2021), The Mars Environmental Dynamics Analyzer, MEDA: A
847 Suite of Environmental Sensors for the Mars 2020 Mission, Space Science Reviews, 217:48,
848 https://doi.org/10.1007/s11214-021-00816-9.
849
850 Schofield, J.T., J.R. Barnes, D. Crisp, R.M. Haberle, S. Larsen, J.A. Magalhaes, J.R. Murphy, A.
851 Seiff, G. Wilson (1997). The Mars Pathfinder Atmospheric Structure Investigation/Meteorology
852 (ASI/MET) Experiment, *Science*, Vol 278 (5344), 1752 – 1758, DOI:
853 10.1126/science.278.5344.1752.
854
855 Smith, C. L., Moores, J. E., Lemmon, M., Guzewich, S. D., Moore, C. A., Ellison, D., &
856 Khayat, A. S. J. (2019). Visibility and line-of-sight extinction estimates in Gale Crater during
857 the 2018/MY34 global dust storm. *Geophysical Research Letters*, 46, 9414– 9421.
858 https://doi.org/10.1029/2019GL083788

859 Smith, M. D., Wolff, M. J., Spanovich, N., Ghosh, A., Banfield, D., Christensen, P. R., Landis,
860 G. A., and Squyres, S. W. (2006), One Martian year of atmospheric observations using MER
861 Mini-TES, *J. Geophys. Res.*, 111, E12S13, doi:10.1029/2006JE002770.

862 Spanovich, N., Smith, M. D., Smith, P., Wolff, M. J., Christensen, P. R., & Squyres, S. W.
863 (2006). Surface and near-surface atmospheric temperatures for the Mars Exploration Rover
864 landing sites. *Icarus*, *180*(2), 314-320. https://doi.org/10.1016/j.icarus.2005.09.014.
865
866 Spiga, A., Forget, F., Dolla, B., Vinatier, S., Melchiorri, R., Drossart, P., Gendrin, A.,
867 Bibring, J.-P., Langevin, Y., and Gondet, B. (2007), Remote sensing of surface pressure on

868 Mars with the Mars Express/OMEGA spectrometer: 2. Meteorological maps, *J. Geophys. Res.*,
869 112, E08S16, doi:10.1029/2006JE002870.
870
871 Steakley, Kathryn, James Murphy (2016). A year of convective vortex activity at Gale crater,
872 *Icarus*, 278, 180-193. http://dx.doi.org/10.1016/j.icarus.2016.06.010.
873
874 Sun, J., Mahrt, L., Nappo, C., & Lenschow, D. H. (2015), Wind and Temperature Oscillations
875 Generated by Wave–Turbulence Interactions in the Stably Stratified Boundary Layer, Journal of
876 the Atmospheric Sciences, 72(4), 1484-1503.
877 https://journals.ametsoc.org/view/journals/atsc/72/4/jas-d-14-0129.1.xml
878
879 Sutton, Jordan L., Conway B. Leovy and James E. Tillman (1978). Diurnal Variations of the
880 Martian Surface Layer Meteorological Parameters During the First 45 Sols at Two Viking
881 Lander Sites, *Jour. Atmos. Sci.*, Vol 35, 2346 – 2355.
882
883 Tilman, J.E. (1988), Mars Global Atmospheric Oscillations Annually Synchronized, Transient
884 Normal-Mode Oscillations and the Triggering of Global Dust Storms Journal of Geophysical
885 Research, no.D8, 9433-9451.
886
887 de la Torre, A., and P. Alexander (1995), The interpretation of wavelengths and periods as
888 measured from atmospheric balloons, J. Appl. Meteorol.,34, 2747–2754.
889
890 de la Torre, A., and P. Alexander (2005), Gravity waves above Andes detected from GPS radio
891 occultation temperature profiles: Mountain forcing?, Geophys. Res. Lett.,32, L17815,
892 doi:10.1029/2005GL022959.
893
894 Torrence, C. and G. P. Compo, 1998: A Practical Guide to Wavelet Analysis, Bull. Amer.
895 Meteor. Soc., 79, 61-78.
896
897 Tyler, D., and Barnes, J. R. (2015), Convergent crater circulations on Mars: Influence on the
898 surface pressure cycle and the depth of the convective boundary layer, *Geophys. Res.*
899 *Lett.*, 42, 7343– 7350, doi:10.1002/2015GL064957.
900
901 Viúdez-Moreiras, D., Newman, C. E., de la Torre, M., Martínez, G., Guzewich, S., Lemmon,
902 M., et al. (2019). Effects of the MY34/2018 global dust storm as measured by MSL REMS in
903 Gale crater. *Journal of Geophysical Research: Planets*, 124, 1899– 1912.
904 https://doi.org/10.1029/2019JE005985
905
906 Viúdez-Moreiras, D., Newman, C. E., Forget, F., Lemmon, M., Banfield, D., & Spiga, A., et
907 al. (2020). Effects of a large dust storm in the near-surface atmosphere as measured by InSight in
908 Elysium Planitia, Mars. Comparison with contemporaneous measurements by Mars Science
909 Laboratory. *Journal of Geophysical Research: Planets*, 125, e2020JE006493.
910 https://doi.org/10.1029/2020JE006493
911
912 Wilson, R. J., and K. Hamilton (1996), Comprehensive model simulation of thermal tides in the
913 Martian atmosphere, *J. Atmos. Sci.*, 53, 1290–1326, doi:10.1175/1520-

0469(1996)053<1290:CMSOTT>2.0.CO;2.

Wilson, John R., Don Banfield, Barney J. Conrath, Michael D. Smith (2002). Traveling waves in the Northern Hemisphere of Mars, *Geophys. Res. Letters.,* 29, 14. http://doi.org/10.1029/2002GL014866.

Whiteman, C. D., 2000, Mountain Meteorology: Fundamentals and Applications. Oxford University Press, 355 pp.

Zurek, R.W. and C.B. Leovy (1981), Thermal tides in the dusty Martian atmosphere: a verification of theory. Science 213(4506), 437–439.